Stability and chemical composition of pargasitic amphibole in MORB pyrolite under upper mantle conditions

Article *in* Contributions to Mineralogy and Petrology · April 1999

DOI: 10.1007/s004100050495

CITATIONS
290

READS
786

2 authors:

Kiyoaki Niida
Hokkaido University
46 PUBLICATIONS **784** CITATIONS

SEE PROFILE

David Headley Green
University of Tasmania
268 PUBLICATIONS **27,564** CITATIONS

SEE PROFILE

Contrib Mineral Petrol (1999) 135: 18–40

K. Niida · D.H. Green

Stability and chemical composition of pargasitic amphibole in MORB pyrolite under upper mantle conditions

Received: 27 October 1997 / Accepted: 6 November 1998

Abstract The stability field of pargasitic amphibole in a model mantle composition (MORB pyrolite) has been experimentally determined for a fixed water content. A solidus for a pargasite-bearing lherzolite has been defined at pressures below the limit of amphibole stability of 30 kbar at $T = 925$ °C. The maximum temperature for pargasitic amphibole in MORB pyrolite occurs at 1075 °C between $P = 18$ and 25 kbar. This maximum lies between that determined for a fertile peridotite composition (Hawaiian pyrolite) and a depleted peridotite composition (Tinaquillo lherzolite). A comparison of the new results with those from earlier studies suggests that the stability for a particular bulk H_2O content is mostly controlled by alkali content of the lherzolite composition. The systematic compositional variation of pargasitic amphibole as a function of pressure and temperature can be represented as an increase of the richterite component with increase in both pressure and temperature. For a given pressure the tschermakite component increases with increasing temperature. The compositions of coexisting clinopyroxenes also show a systematic variation with pressure and temperature. The phase relationships in MORB pyrolite combined with the modal abundance of coexisting phases show that the breakdown reactions of pargasitic amphibole occur continuously throughout the subsolidus region studied. The temperature stability limit of pargasitic amphibole coincides with the water-undersaturated solidus (amphibole-dehydration solidus) at pressures below 30 kbar. The experimental results are applicable to pargasitic amphibole-bearing natural peridotites. Cooling and decompression paths and heating events observed in natural peridotites can be interpreted from changes in the composition of pargasitic amphibole. The data are also applicable to a model for peridotite melting and hydration process in the subduction environment.

K. Niida (✉)
Department of Earth and Planetary Science,
Hokkaido University,
W-8, Sapporo 060-0810, N-10, Japan

D.H. Green
Research School of Earth Science,
Australian National University,
Canberra ACT 0200, Australia

Editorial responsibility: V. Trommsdorff

Introduction

Pargasitic amphiboles are well known in upper mantle-derived spinel and garnet lherzolite xenoliths (e.g. Varne 1970; Francis 1976; Takahashi 1980; Dawson and Smith 1982; Griffin et al. 1984; Nickel and Green 1984; Neal and Nixon 1985; Press et al. 1986; Fabriès et al. 1987; Dautria et al. 1987; Field et al. 1989) and in orogenic lherzolites tectonically emplaced within crustal terrains (e.g. Green 1964; Cawthorn 1975; Ernst 1978; Medaris 1980, 1984; Obata 1980; Obata and Morten 1987; Seyler and Mattson 1989). Because of its world-wide occurrence, pargasitic amphibole has been recognized as a ubiquitous hydrous phase in the Earth's uppermost mantle.

Previous experimental studies indicate that pargasitic amphiboles are stable up to 25–30 kbar at subsolidus conditions and up to 950–1000 °C in various peridotite compositions with excess water (Kushiro 1970; Green 1973; Millhollen et al. 1974; Mysen and Boettcher 1975a, b; Mengel and Green 1989; Wallace and Green 1991). Under water-undersaturated conditions the maximum temperature of amphibole stability increases up to 1025 °C for Tinaquillo lherzolite composition (Wallace and Green 1991) and up to 1150 °C for Hawaiian pyrolite (Green 1973) and NHD (Northern Hessian Depression) peridotite (Mengel and Green 1989) compositions. These studies have demonstrated the importance of bulk composition in determining both the pargasite composition and solidus temperatures for pargasite-bearing lherzolite.

The natural processes of sampling of the Earth's upper mantle, by xenolith suites, by tectonically or

diapirically emplaced orogenic lherzolites and by primary magmas, all confirm the presence of significant and variable quantities of water (hydrogen) in minerals or melts from the mantle. It has been shown that the *P-T* location of the mantle solidus is extremely sensitive to amphibole stability relationships under fluid-absent or fluid-present conditions (Green 1973; Holloway 1973). Similarly, one of the processes commonly invoked for the decomposition of pargasitic amphibole is change in activity of water (a_{H_2O}). In this paper, we report an experimental study of amphibole stability in the MORB pyrolite composition to further constrain partial melting and metasomatic processes in the Earth's upper mantle.

Experimental approach and techniques

In studies of the Earth's upper mantle the term "pyrolite" (Ringwood 1962; Green and Ringwood 1963) has been applied to model mantle compositions which are lherzolitic and calculated by combining a primitive basalt with a harzburgite residue. The composition used in this study is a model "MORB (mid ocean ridge basalt) pyrolite" (MPY; in Table 1) calculated by Green et al. (1979). The calculation was based on combining 24 wt% of the MOR picrite composition [83% DSDP (Deep Sea Drilling Project) 3-18-7-1 plus 17% olivine: Mix E; Green et al. 1979], which is in equilibrium with olivine + orthopyroxene at 20 kbar, 1430 °C, with 76 wt% harzburgite. The MORB pyrolite composition was constructed as a geochemically appropriate source composition for the production of primary MORB magma (Green et al. 1979, 1987), and its melting behaviour as a function of pressure and temperature has been fully explored under anhydrous conditions (Falloon and Green 1987, 1988; Falloon et al. 1988). The MORB pyrolite is intermediate in composition between "Hawaiian pyrolite (HPY)", which represents a fertile or enriched peridotite (Green 1973), and "Tinaquillo lherzolite (TQ)", which represents a refractory or depleted peridotite (Jaques and Green, 1979, 1980) in terms of incompatible elements but is not depleted in Ca and Al (i.e. it is a lherzolitic and not a harzburgitic composition).

For the experiments, 40 wt% olivine ($Mg_{91.6}Fe_{8.1}Ni_{0.2}Mn_{0.1}$) was subtracted from the MORB pyrolite composition in order to increase the modal abundance of minor phases such as pyroxenes, amphibole, spinel, garnet and melt (MPY −40%OL; in Table 1). This composition has been used in partial melting experiments under anhydrous conditions by Falloon and Green (1987, 1988) and Falloon et al. (1988).

The starting mix was prepared from analytical grade oxides and carbonates, ground under acetone, and sintered at 950 °C. Ferrous iron was then added as Fe_2SiO_4 (fayalite) to this mix and the mix was fired at 450 °C in an Ar-atmosphere. For the preparation of starting material that contains pargasites but no excess water and is to be used for experimental runs under water-undersaturated conditions, 100 mg batches of this mix were loaded into large-capacity $Ag_{50}Pd_{50}$ capsules with 2 wt% water. The water was added to the capsule by microsyringe and checked by weighing the capsule before and after sealing, and also after the run. After the water-presaturated mixture had been run at 15 kbar, 925 °C for 48 h, the quenched product was finely crushed and mixed under acetone, then dried at 250 °C. Prepared in this manner, the starting material is composed of a fine-grained subsolidus assemblage of olivine + orthopyroxene + clinopyroxene + spinel + amphibole (amphibole-bearing spinel lherzolite). The mineralogy and vapor-saturated subsolidus character were confirmed by electron microprobe analyses of all five phases and by SEM photography of the freshly broken surface. The amount of water fixed in amphiboles in the starting material is approximately 0.6% (see modal proportion in Table 4), assuming 1.8 wt% H_2O in pargasite (Green 1964), or 0.7%, if pargasite contains ~2.2 wt% H_2O. Approximately 15 mg portions of the large-capacity run product were used in each subsequent run at various *P*, *T* conditions, using small-capacity $Ag_{75}Pd_{25}$ or $Ag_{50}Pd_{50}$ capsules.

All experiments under water-undersaturated condition, listed in Table 2, were carried out in a high pressure piston-cylinder apparatus at the University of Tasmania or at the Australian National University, using a piston-in technique. As a NaCl or a NaCl-Pyrex glass sleeve was used in the 12.7 mm diameter furnace assembly, no friction correction was applied. From calibration experiments, the stated pressures are considered to be accurate to within 0.5 kbar. Small-capacity $Ag_{75}Pd_{25}$ capsules were used for runs at higher

Table 1 Chemical compositions of MORB pyrolite and other peridotite compositions used for experiments on pargasitic amphibole stability. [*FeO** total iron as FeO*, Mg# Mg/(Mg + Fe*), *1 MPY* MORB pyrolite composition (Green et al. 1979), *2 MPY* −40%OL MORB pyrolite (*MPY*) minus 40 wt% olivine (Mg91.6Fe8.1Ni0.2Mn0.1), *3 HPY* Hawaiian pyrolite composition (Green 1973), *4 HPY* −40%OL Hawaiian pyrolite (*HPY*) minus 40 wt% olivine (Mg91.6Fe8.1Ni0.2Mn0.1), *5 TQ* Tinaquillo lherzolite (Jaques and Green 1980), 6 *TQ* −40%OL Tinaquillo lherzolite (*TQ*) minus 40 wt% olivine (Mg91.9Fe8.0Mn0.1), *7 NHD* Northern Hessian Depression peridotite (Mengel and Green 1989), *8 NHD+1.5%PHL* −40%OL NHD peridotite plus 1.5% phlogopite minus 60 wt% olivine (Fo89.9)]

	1 MPY	2 MPY −40%OL	3 HPY	4 HPY −40%OL	5 TQ	6 TQ −40%OL	7 NHD	8 NHD +1.5%PHL −60%OL
SiO_2	44.74	47.15	45.20	47.90	44.95	47.50	43.40	47.20
TiO_2	0.17	0.28	0.71	1.18	0.08	0.13	0.08	0.25
Al_2O_3	4.37	7.28	3.54	5.91	3.22	5.35	2.00	5.60
FeO*	7.55	7.27	8.47	8.81	7.66	7.51	8.60	6.69
MnO	0.11	0.12	0.14	0.13	0.14	0.18	0.13	0.07
MgO	38.57	30.57	37.50	28.80	40.03	32.80	43.10	33.59
CaO	3.38	5.63	3.08	5.14	2.99	4.97	1.80	4.43
Na_2O	0.40	0.66	0.57	0.95	0.18	0.30	0.13	0.35
K_2O	0.00	0.00	0.13	0.22	0.02	0.03	0.03	0.43
P_2O_5	0.00	0.00	0.04	0.06	0.01	0.02	–	–
Cr_2O_3	0.45	0.75	0.43	0.72	0.45	0.75	0.30	1.08
NiO	0.26	0.29	0.20	0.13	0.26	0.43	0.42	0.30
Total	100.00	100.00	100.01	99.95	99.99	99.97	99.99	99.99
Mg#	0.901	0.882	0.888	0.853	0.903	0.886	0.899	0.899

pressures, and $Ag_{50}Pd_{50}$ capsules were used for runs at lower pressure or higher temperatures. Temperatures were automatically controlled to within 2 °C of the set point by EUROTHERM 818P or Kent P96 M controllers using a $Pt/Pt_{90}Rh_{10}$ thermocouple. No oxygen buffer was used. The f_{O_2} estimates for the subsolidus olivine + orthopyroxene + spinel assemblages using the Ballhaus et al. (1990) calibration show that the f_{O_2} for subsolidus runs was in the FMQ (fayalite-magnetite-quartz) to WM (wüstite-magnetite) range. An additional series of 925 °C runs was performed under water-saturated conditions, using the same techniques as in the experiments to synthesize starting mix assemblage, in order to obtain reasonably coarse-grained run products, saturated with water vapor and below the silicate solidus.

All the experimental run products were examined microscopically in immersion oils, enabling recognition of all major phases including the distinctive amphibole prisms. Small discs recovered from the capsules were polished for microprobe analysis. The analyses were done mostly on a JEOL-JX50A electron microprobe (University of Tasmania) fitted with an energy dispersive EDAX system, operating at 15 kV, 7×10^{-10} A, using a pure Cu calibration. The analyses for the water-saturated runs at $T = 925$ °C were carried out on the SEM (JSM-6400) fitted with an energy dispersive EDX system operating at the Electron Microscopy Unit, ANU. Phase identification and textural and compositional homogeneity of phases were also checked by scanning electron microscopy images using back-scattered electrons on the SEM. Defocused beam microprobe analyses of bulk composition and analyses (Mg#) of silicate phases confirmed that Fe-loss to the capsule walls was negligible under the chosen run conditions.

With the experimental method chosen, we are treating H_2O as an additional oxide, present in the charge in a fixed amount, determined by the initial synthesis. The addition of water causes the appearance of an additional phase, amphibole or fluid, or water dissolves in melt at higher temperatures. We anticipate that phases, including amphibole, will change in composition and proportions as a function of pressure and temperature and that mass balance calculations will require each component to be conserved. This becomes important in interpreting our results because the presence or absence of a H_2O-rich fluid is difficult to detect by the quenching method and we have resorted to scanning and transmission electron microscopy for this purpose. In our experiments, melting occurs at a multiphase "eutectic" among the crystalline phases with pargasite showing incongruent melting behavior at $P < 30$ kbar. Also H_2O-rich fluid will be present at pressures higher than the amphibole stability limit, and at these pressures (>30 kbar) melting is water saturated at the solidus. At lower pressures, because the amount of water in the charge is small (0.6 wt%) and the water solubility in silicate melts at ≥5 kbar is high and increases with pressure, we expect all water to enter the melt at the solidus or very close to the solidus. In fact the amount of melt at the dehydration solidus may be estimated from the solubility of water in basaltic melt as a function of pressure and temperature.

Experimental results

1. Dehydration solidus of pargasite-bearing MORB pyrolite

Experimental run details are listed in Table 2. The phase relationships for MORB pyrolite composition (MPY -40%OL) under water-undersaturated condition ($P_{H_2O} < P_{total}$) are summarized in Fig. 1. The water-undersaturated solidus curve of MORB pyrolite shows a convex shape similar to those determined for other peridotite compositions (Green 1973; Millhollen et al. 1974; Mysen and Boettcher 1975a, b; Mengel and Green 1989; Wallace and Green 1991). The position of the solidus is based on optical and SEM recognition of interstitial quenched melt and quench outgrowth of residual phases. The SEM and TEM images also confirmed the solidus and the contrast between the crystals + vapor assemblage below the solidus and the crystals and quenched silicate melt above the solidus (Figs. 2 and 3).

Pargasitic amphiboles are present in all subsolidus runs at pressures below 30 kbar. Experimental runs within 10–20 °C above the solidus still contain visible amounts of amphibole with quenched melt. As shown in Fig. 1, the upper stability limit of the amphibole is approximately 15 °C above the solidus. Due to the near coincidence of the solidus and the amphibole breakdown, the solidus can conveniently be described as an amphibole-dehydration solidus (Green 1973; Green et al. 1987), in contrast to solidi in the presence of subsolidus, water-rich fluid phases or in anhydrous compositions.

Lherzolite phase assemblages of olivine + orthopyroxene + clinopyroxene ± garnet ± spinel ± plagioclase were observed in all experimental charges ($P = 4$–32 kbar, $T = 925$–1100 °C). Garnet appears at $P > 20$ kbar between $T = 1000$–1100 °C. Both garnet and spinel were observed in the three charges at $P = 20$ kbar, $T > 1000$ °C. Minute granules of spinel (<1 μm) are still included in amphibole, olivine and pyroxenes at pressures ≥23 kbar. It is uncertain whether the spinel inclusions are relict and metastable or whether they are stable because they are very Cr-rich spinels. Mass balance calculations do not indicate any significant amount of Cr-rich spinels. It is assumed that the field of coexistence of garnet and Al-Cr spinel is limited to $P < 22$ kbar and $T < 1100$ °C. The runs at pressures below 7 kbar contain small amounts of plagioclase, which becomes unstable by 10 kbar. Phlogopite was not present in any experimental runs studied because of the K_2O-free nature of the starting mix (Table 1) and the pargasite does not approach K-saturation as in the experiments of Mengel and Green (1989).

2. Chemical composition of minerals

Olivine

The Mg# [Mg# = 100 Mg/(Mg + Fe*); Fe* = total iron] of olivine varies from 86.4 to 90.2 (Table 3A). In most cases, olivine has a higher Mg# than the initial mix (MPY-40%OL; Mg# = 88.2). This is attributed to minor Fe^{3+} in spinel and amphibole and to Fe/Mg partitioning among olivine, pyroxenes, spinel, garnet and amphibole.

The Mg# of olivine increases with increasing pressure. In detail, subsolidus olivines at $P \leq 18$ kbar have Mg# ≤ 88.8, but subsolidus olivines at $P \geq 20$ kbar have Mg# increasing with pressure to Mg# = 89.5–89.9 at $P = 27$–32 kbar. This is attributed to the appearance and increase in modal abundance of garnet, from 8% to 30%, particularly at $P \geq 25$ kbar. As garnet has Mg# = 76.3–82.8, it has the effect of moving the coexisting phases to higher Mg# in a constant bulk compo-

Table 2 Results of experiments on amphibole-bearing MORB pyrolite. (*S.M.* starting materials, *Ol* olivine, *Opx* orthopyroxene, *Cpx* clinopyroxene, *Sp* spinel, *Ga* garnet, *Pl* plagioclase, *Am* amphibole, *gl* quenched glass, *small amounts)

Run no.	*P* (kbar)	*T* (°C)	Time (h)	H_2O (wt%)	S.M.	Phases identified
Starting materials for water-undersaturated runs						
T-2613	15	925	48	2.0	(A)	Ol, Opx, Cpx, Sp, Am
T-2641	15	925	48	2.0	(B)	Ol, Opx, Cpx, Sp, Am
T-2669	15	925	48	2.0	(C)	Ol, Opx, Cpx, Sp, Am
T-2700	15	925	48	2.0	(D)	Ol, Opx, Cpx, Sp, Am
T-2714	15	925	48	2.0	(E)	Ol, Opx, Cpx, Sp, Am
T-2808	15	925	48	2.0	(F)	Ol, Opx, Cpx, Sp, Am
T-2854	15	925	48	2.0	(G)	Ol, Opx, Cpx, Sp, Am
Water-undersaturated runs						
T-2729	4	1000	94		E	Ol, Opx, Cpx, Sp, Pl, gl*
T-2738	5	975	96		E	Ol, Opx, Cpx, Sp, Pl, Am
T-2721	7	1025	73		E	Ol, Opx, Cpx, Sp, Pl, Am*, gl*
T-2708	7	1050	48		D	Ol, Opx, Cpx, Sp, Pl, gl
T-2643	10	1000	72		B	Ol, Opx, Cpx, Sp, Am
T-2649	10	1050	48		B	Ol, Opx, Cpx, Sp, Am*, gl*
T-2646	10	1075	26.5		B	Ol, Opx, Cpx, Sp, gl
T-2665	10	1100	6		B	Ol, Opx, Cpx, Sp, gl
T-2712	15	1050	48		D	Ol, Opx, Cpx, Sp, Am
T-2709	15	1075	42		D	Ol, Opx, Cpx, Sp, gl*
T-2818	18	1050	48		F	Ol, Opx, Cpx, Sp, Am
T-2813	18	1075	28		F	Ol, Opx, Cpx, Sp, Am*, gl*
T-2814	18	1100	24		F	Ol, Opx, Cpx, Sp, gl
T-2817	20	1050	48		F	Ol, Opx, Cpx, Ga, Sp, Am
T-2717	20	1075	30		E	Ol, Opx, Cpx, Ga, Sp, Am*, gl*
T-2624	23	1075	27		A	Ol, Opx, Cpx, Ga, Am
T-2616	20	1100	24		A	Ol, Opx, Cpx, Ga, Sp, gl*
T-2693	24	1075	29.5		C	Ol, Opx, Cpx, Ga, Am*, gl*
T-2705	24	1100	24		D	Ol, Opx, Cpx, Ga, gl
T-2626	25	1000	71		A	Ol, Opx, Cpx, Ga, Am
T-2672	25	1075	28		C	Ol, Opx, Cpx, Ga, Am*, gl*
T-2677	26	1050	48		C	Ol, Opx, Cpx, Ga, Am*, gl*
T-2703	26	1075	24		D	Ol, Opx, Cpx, Ga, gl
T-2663	27	1000	70		B	Ol, Opx, Cpx, Ga, Am
T-2632	27	1025	48		A	Ol, Opx, Cpx, Ga, Am*, gl*
T-2621	27	1100	23		A	Ol, Opx, Cpx, Ga, gl
T-2635	28	1000	72		A	Ol, Opx, Cpx, Ga, Am
925 °C runs under water-saturated and -undersaturated conditions						
C3	5	925	96	>3.0		Ol, Opx, Cpx, Sp, Pl, Am
C4	10	925	96	>3.0		Ol, Opx, Cpx, Sp, Am
T-3643	20	925	72		G	Ol, Opx, Cpx, Sp, Am
T-3644	25	925	69		G	Ol, Opx, Cpx, Ga, Am
C5	28	925	120	>3.0		Ol, Opx, Cpx, Ga, Am
C6	30	925	120	>3.0		Ol, Opx, Cpx, Ga, Am
C7	32	925	96	>3.0		Ol, Opx, Cpx, Ga
C8	32	925	336	<0.5		Ol, Opx, Cpx, Ga

sition. Subsolidus experiments have olivine with Mg# = 86.4–88.8 at ≤18 kbar, whereas runs above the solidus and lacking amphibole have olivine with Mg# = 89.0–90.2 over this pressure range. At $P = 10$ kbar, a run 50 °C above the solidus has olivines with Mg# = 90.2. This is attributed to partial melting, and the relatively large amount of melting controlled by water solubility and temperature at lower pressure. The olivine contains 0.30 to 0.76 wt% NiO, showing no systematic variations with temperature and pressure.

Orthopyroxene

Orthopyroxene compositions of MORB pyrolite have En, Fs, and Wo ranges of $En_{85.6–89.6}$, $Fs_{9.8–12.6}$, and $Wo_{0.6–2.9}$. As with olivine, the Mg# of orthopyroxene increases with increasing temperature and pressure from 89.0 ($P = 15$ kbar, $T = 925$ °C) to 90.5 ($P = 32$ kbar, $T = 925$ °C) and 90.1 ($P = 27$ kbar, $T = 1050$ °C). The Mg# of orthopyroxene from the above-solidus runs is slightly higher than that from the subsolidus runs (Table 3B).

Total Al_2O_3 and Al^{VI}/Al^{IV} increase with increasing temperature. A marked drop of Al_2O_3 and Al^{VI}/Al^{IV} with increasing pressure is observed in the garnet stability field. The Ca/(Ca + Mg) of orthopyroxene smoothly increases with increasing temperature, except for orthopyroxene from the $T = 925$ °C runs, which has unexpectedly high or low concentration of CaO attributed to analytical difficulty in this fine-grained material. The Ca/(Ca + Mg) of orthopyroxene from the spinel lherzolite

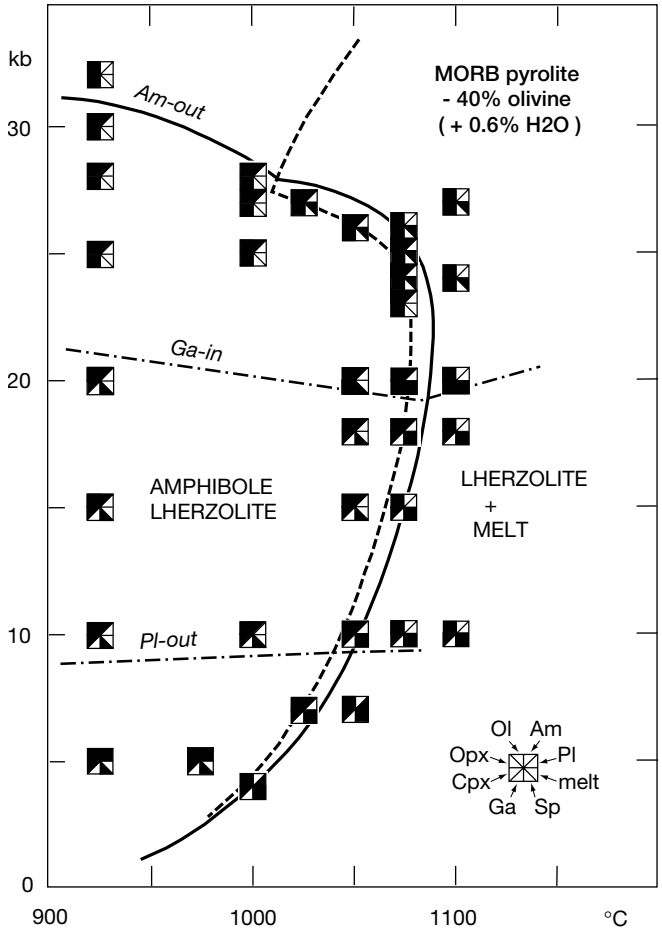

Fig. 1 Experimental results defining the water-undersaturated solidus (*dashed line*) and the amphibole stability limit (*heavy line*) of MORB pyrolite –40% olivine composition with approximately 0.6 wt% H_2O. *Box symbols* show the phase relationships (*Ol* olivine, *Opx* orthopyroxene, *Cpx* clinopyroxene, *Ga* garnet, *Sp* spinel, *melt* glass, *Pl* plagioclase, *Am* amphibole). *Dashed lines with dots* are the reaction curves for garnet-in (*Ga-in*) and plagioclase-out (*Pl-out*)

field shows a slight increase with increasing pressure, whereas in the garnet-lherzolite field a rapid decrease of Ca/(Ca + Mg) with increasing pressure is detectable.

The Cr content of orthopyroxene increases slightly with increasing temperature, as observed in experiments by Kushiro et al. (1972) and Mysen and Boettcher (1975a, b). Unusually high Cr contents of orthopyroxenes observed in some analyses can be explained by the presence of tiny spinel inclusions.

Clinopyroxene

Clinopyroxene in the MORB pyrolite has a wider range in Mg#, from 88.1 to 91.9, with values higher than those of olivine and orthopyroxene (Table 3C). Anomalously low values of Mg#, however, for examples at $P = 10$ kbar, $T = 1100$ °C, and $P = 18$ kbar, $T = 1100$ °C, which show reversals of trend from lower temperature runs, are attributed to quench rims on the clinopyroxene cores.

Under subsolidus conditions there is a clear positive correlation of Na content of clinopyroxene with increasing pressure. This is weakly displayed in the spinel lherzolite field but clearly evident in the garnet lherzolite field. There appears to be a slight positive correlation between Na content and Al^{VI}/Al^{IV} with temperature, but the clinopyroxene analyses just above the solidus which show higher Na content are affected by probable admixture of a small component of quench outgrowth included in the microprobe analysis. Although Al^{VI}/Al^{IV} increases with increasing pressure in the subsolidus runs the total Al content of clinopyroxene decreases, particularly in the garnet lherzolite field. This is attributed to replacement of the Tschermak's molecule in pyroxene by garnet at higher pressure. The maximum Tschermak's component in clinopyroxene (i.e. minimum Si^{IV}) is attained in the 10–18 kbar experiments, at temperatures immediately above the solidus, i.e. 1050–1100 °C. The TiO_2 content of clinopyroxene (0.19–0.48 wt%) appears to vary in parallel with Tschermak's component, i.e. a positive correlation with temperature and a negative correlation with pressure.

Pargasite

The amphibole compositions from both subsolidus and near-solidus runs of MORB pyrolite are pargasitic (Table 3D). The Mg# of pargasitic amphibole ranges from 86.2 to 90.4, and increases with increasing pressure and temperature.

Compositional variations observed in the pargasitic amphiboles generally can be explained in terms of substitutions based on the structural formula of tremolite [• $Ca_2Mg_5Si_8O_{22}(OH)_2$, where • = vacancy in the A-site]. The simple cation exchanges active in the experimental runs on MORB pyrolite are $Mg = Fe^{2+}$ in the M1-M3-site and $Ca = Fe^{2+}$ in the M4 site. A-site occupancy by K is negligible in the MORB pyrolite amphiboles because of the K_2O-free nature of the initial starting mix.

The coupled substitutions occurring in the experimentally produced amphiboles from MORB pyrolite are as follows:

$Al_2\ Mg_{-1}\ Si_{-1}$ (ts: tschermakite)
$Ti\ Al_2\ Mg_{-1}\ Si_{-2}$ (Ti-ts: Ti-tschermakite)
$Cr\ Al\ Mg_{-1}\ Si_{-1}$ (Cr-ts: Cr-tschermakite)
$Fe^{3+}\ Al\ Mg_{-1}\ Si_{-1}$ (Fe-ts: ferri-tschermakite)
$Na\ Al\ \bullet_{-1}\ Si_{-1}$ (ed: edenite)
$Na\ Na\ \bullet_{-1}\ Ca_{-1}$ (ri: richterite)
$Na\ Al\ Ca_{-1}\ Mg_{-1}$ (gl: glaucophane)

The TiO_2 content of pargasitic amphibole varies with increasing temperature from 0.53 to 1.23 wt%. The Ti-ts component, however, slightly decreases with increasing pressure. The Cr_2O_3 content of pargasitic amphibole ranges from 0.75 to 1.47 wt%, and our data does not reveal any systematic variations with pressure and temperature.

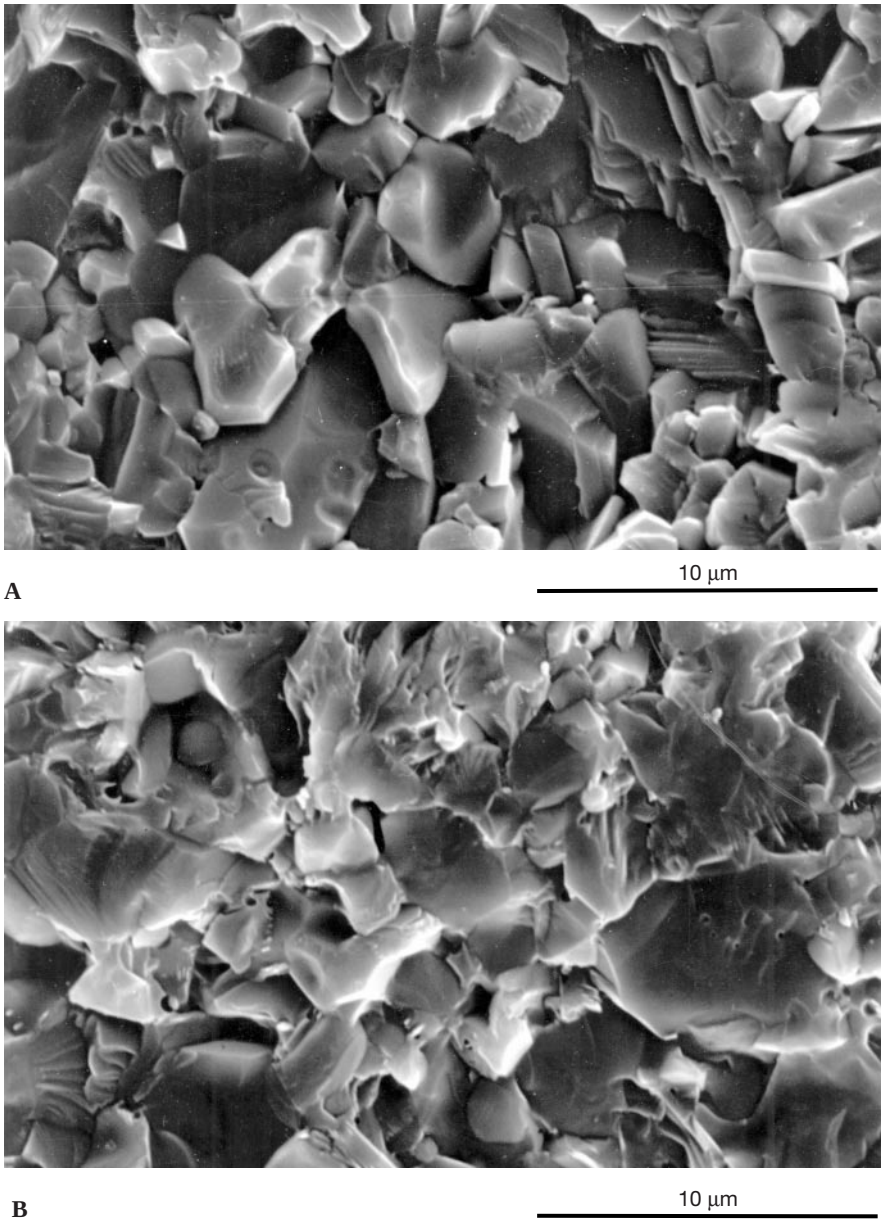

Fig. 2A, B Scanning electron microscope (SEM) images of freshly broken surfaces of experimental charges at $P = 10$ kbar, $T = 1000$ °C (**A**), and at $P = 10$ kbar, $T = 1050$ °C (**B**). Scale *bar* is 10 micron. SEM image **A** is subsolidus with euhedral growth faces on crystals often breaking cleanly against voids (intergranular fluid). **B** is above-solidus with quench crystal growth and intergranular glass, producing "welded" primary grains and conchoidal fracture surfaces

Total Na (A and M4) of pargasitic amphibole increases with increasing pressure, as shown in Fig. 4A. The data suggest that the P versus Na-total plot of Fig. 4A can be contoured for constant temperature and that the isotherms are kinked at the first appearance of spinel and garnet. The total Na also increases with increasing temperature at a fixed pressure (Fig. 4B). The M4-site occupancy by Na becomes more important in the garnet lherzolite field (Fig. 5), where the Na/Ca ratio of pargasite increases more rapidly with increasing pressure. At a given pressure, the Na/Ca also increases with increasing temperature. The total Na can be described in terms of the A-site occupancy, which is the sum of $Na(A)_{edenite} + Na(A)_{richterite}$, and the M4 site occupancy, which is the sum of $Na(M4)_{richterite} + Na(M4)_{glaucophane}$. The total Na and Na(M4) variations of the pargasitic amphiboles suggest that the edenite and richterite substitutions become more prominent with increasing pressure and temperature, and that the richterite substitution becomes particularly significant in the garnet stability field (Figs. 4 and 5).

The total Al and Al^{VI}/Al^{IV} of the pargasitic amphibole both increase with increasing temperature (Table 3D), in particular in the spinel lherzolite (Fig. 5). This suggests that the tschermakite (ts) component becomes more significant relative to the richterite (ri) component with increasing temperature. The increasing trend of Al^{IV} with temperature has been shown in experimentally produced pargasitic amphiboles (Holloway and Burnham 1972; Helz 1973; Spear 1981).

The changes in Na and Al of the MORB pyrolite amphiboles may be summarized as increasing richterite component with increasing pressure and increasing Tschermak's component at higher temperatures. These

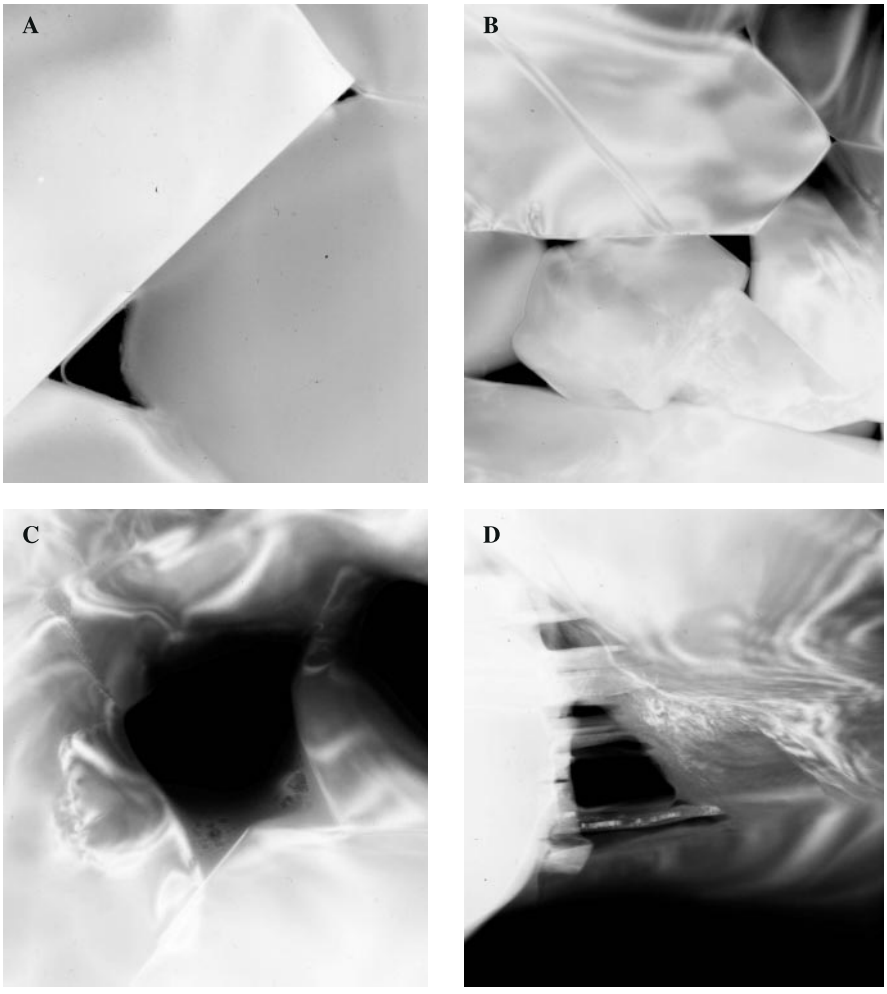

Fig. 3A–D Transmission electron microscope (TEM) images of ion-beam thinned samples of experimental run products: **A** 10 kbar, 1000 °C run (No. 2643; also illustrated in Fig. 2A). Subsolidus run with voids between crystal faces. The voids were occupied by fluid which has quenched to yield a delicate thin glass film in the corner of the larger void. **B** 27 kbar, 1000 °C run (No. 2663). Grain boundaries are "dry" in the sense of silicate melt or quench crystalline phases but the presence of voids (fluid-filled cavities at the P, T conditions of the experiment) is characteristic. **C** 10 kbar, 1050 °C run (No. 2649; also illustrated in Fig. 2B). The intergranular space is rimmed by quench crystal outgrowth (from semiquantitative EDS analysis) and contains a quench modified silica-rich and alkali-rich glass. The hole within the glass is a consequence of ion-beam thinning. **D** 10 kbar, 1050 °C run (No. 2649), showing a quench filling of an intergranular space between primary crystals with quench outgrowth. The quench phase is a hydrous phyllosilicate. Other quench phases show layers, indicating quench amphibole of contrasting composition to primary amphibole in the charge

changes are summarized in Figs. 4 and 5, which emphasize the capacity of the amphibole structure to accommodate P, T changes by continuous solid solution. The glaucophane substitution is not important at our experimental conditions in the MORB pyrolite amphiboles, judging from the independent variations of Na(M4) and Al^{VI}.

Garnet

Garnet from the MORB pyrolite experiments is pyrope rich with a Mg# ranging from 76.2 to 82.8 (Table 3E). The Mg# increases with increasing temperature at a constant pressure. A positive correlation between the Ca/(Ca + Mg) ratio and temperature is also observed, except for garnet from the $T = 925$ °C runs, which has high content of CaO. The Ca/(Ca + Mg) ratio varies from 0.17 to 0.24. There is no observable pressure dependence of either the Mg/(Mg + Fe*) or Ca/(Ca + Mg) ratios.

The Cr_2O_3 and Al_2O_3 contents of garnet in the spinel-free experimental charges range 0.84 to 2.46 wt% and 20.50 to 23.67 wt%, respectively.

Spinel

Spinel is observed as small granules, mostly less than 1 μm in diameter. In some experimental runs near the solidus, the grain size of spinel attains more than 2 μm. Due to the small grain size of spinel it was difficult to obtain microprobe analyses but the data obtained show that the Mg# of spinel ranges from 70.3 to 84.9, and increases with increasing temperature (Table 3F). The Cr# [Cr# = 100Cr/(Cr + Al)] varies from 13.2 to 29.9 and decreases with increasing temperature.

Plagioclase

Plagioclase was observed as small prismatic grains in the experimental charges at pressures below 7 kbar. The plagioclase grains are generally less than 5 μm in diameter, and are mostly in contact with quench glass in the above-solidus runs. Due to the difficulty in obtaining microprobe analyses of plagioclase, the equilibrium plagioclase composition could not be determined with any certainty. The plagioclase crystallized at $T = 925$ °C and $P = 5$ kbar has a composition near $An_{92.5}$ (Table 3F).

Table 3A Representative electron microprobe analyses (EDS) of olivines from experiments on MORB pyrolite

Run no.	C3	C4	T-2700	T-3643	T-3644	C5	C6	C7	C8	T-2738	T-2729	T-2643	T-2626	T-2663	T-2635	T-2721	T-2632	T-2708
T °C	925	925	925	925	925	925	925	925	925	975	1000	1000	1000	1000	1000	1025	1025	1050
P	5	10	15	20	25	28	30	32	32	5	4	10	25	27	28	7	27	7
SiO_2	40.17	39.93	41.32	40.06	40.46	40.52	40.62	40.64	40.62	40.77	41.03	40.88	41.21	41.26	41.42	40.79	40.77	41.07
FeO	12.49	12.21	10.72	11.14	10.80	11.10	10.76	9.78	9.85	11.07	10.55	11.05	10.56	10.01	10.03	10.67	9.94	10.43
NiO	0.56	0.54	0.40	0.50	0.69	0.58	0.69	0.76	–	0.39	0.46	0.51	0.39	0.50	0.64	0.46	0.67	0.43
MgO	46.68	47.25	47.56	48.30	47.99	47.41	47.84	48.76	49.39	47.77	47.95	47.56	47.83	48.22	47.90	48.08	48.62	48.08
CaO	0.10	0.06	0.00	0.00	0.06	0.38	0.09	0.06	0.14	0.00	0.00	0.00	0.00	0.00	0.00	0.00	0.00	0.00
Total	100.00	100.00	100.00	100.00	100.00	100.00	100.00	100.00	100.00	100.00	100.00	100.00	100.00	100.00	100.00	100.00	100.00	100.00
(O = 4)																		
Si	0.999	0.992	1.015	0.990	0.998	1.001	1.002	0.999	0.995	1.005	1.009	1.008	1.012	1.012	1.016	1.004	1.001	1.009
Fe	0.260	0.254	0.220	0.230	0.223	0.229	0.222	0.201	0.202	0.228	0.217	0.228	0.217	0.205	0.206	0.220	0.204	0.214
Ni	0.011	0.011	0.008	0.010	0.014	0.012	0.014	0.015	–	0.008	0.009	0.010	0.008	0.010	0.013	0.009	0.013	0.008
Mg	1.729	1.750	1.741	1.779	1.765	1.746	1.759	1.785	1.804	1.755	1.757	1.747	1.751	1.762	1.750	1.764	1.780	1.760
Ca	0.003	0.002	0.000	0.000	0.002	0.010	0.002	0.002	0.004	0.000	0.000	0.000	0.000	0.000	0.000	0.000	0.000	0.000
Total	3.001	3.008	2.985	3.010	3.002	2.999	2.998	3.001	3.005	2.995	2.991	2.992	2.988	2.988	2.984	2.996	2.999	2.991
Mg#	86.95	87.33	88.77	88.54	88.79	88.39	88.79	89.88	89.94	88.49	89.01	88.47	88.98	89.57	89.48	88.93	89.71	89.15

Run no.	T-2649	T-2712	T-2818	T-2817	T-2677	T-2646	T-2709	T-2813	T-2717	T-2624	T-2693	T-2672	T-2703	T-2665	T-2814	T-2616	T-2705	T-2621
T °C	1050	1050	1050	1050	1050	1075	1075	1075	1075	1075	1075	1075	1075	1100	1100	1100	1100	1100
P	10	15	18	20	26	10	15	18	20	23	24	25	26	10	18	20	24	27
SiO_2	40.92	40.93	40.72	40.65	41.08	41.03	40.75	40.67	40.87	40.91	41.06	41.04	41.06	41.34	40.77	41.09	41.10	40.98
FeO	10.75	10.79	10.92	10.62	9.94	10.16	10.75	10.53	10.33	10.59	9.89	10.00	9.61	9.48	10.20	10.33	9.56	10.15
NiO	0.41	0.41	0.59	0.50	0.49	0.44	0.35	0.61	0.30	0.35	0.54	0.40	0.42	0.48	0.49	0.40	0.44	0.50
MgO	47.93	47.87	47.77	48.24	48.48	48.37	48.15	48.18	48.50	48.15	48.51	48.56	48.91	48.70	48.54	48.18	48.90	48.37
CaO	0.00	0.00	0.00	0.00	0.00	0.00	0.00	0.00	0.00	0.00	0.00	0.00	0.00	0.00	0.00	0.00	0.00	0.00
Total	100.00	100.00	100.00	100.00	100.00	100.00	100.00	100.00	100.00	100.00	100.00	100.00	100.00	100.00	100.00	100.00	100.00	100.00
(O = 4)																		
Si	1.007	1.007	1.004	1.001	1.007	1.007	1.003	1.001	1.004	1.006	1.007	1.006	1.005	1.011	1.002	1.009	1.006	1.006
Fe	0.221	0.222	0.225	0.219	0.204	0.209	0.221	0.217	0.212	0.218	0.203	0.205	0.197	0.194	0.210	0.212	0.196	0.208
Ni	0.008	0.008	0.012	0.010	0.010	0.009	0.007	0.012	0.006	0.007	0.011	0.008	0.008	0.009	0.010	0.008	0.009	0.010
Mg	1.757	1.756	1.755	1.770	1.772	1.769	1.766	1.768	1.775	1.764	1.773	1.774	1.785	1.775	1.777	1.763	1.784	1.770
Ca	0.000	0.000	0.000	0.000	0.000	0.000	0.000	0.000	0.000	0.000	0.000	0.000	0.000	0.000	0.000	0.000	0.000	0.000
Total	2.993	2.993	2.996	2.999	2.993	2.993	2.997	2.999	2.996	2.994	2.993	2.994	2.995	2.989	2.998	2.991	2.994	2.994
Mg#	88.82	88.77	88.63	89.00	89.68	89.46	88.87	89.08	89.32	89.01	89.73	89.64	90.07	90.15	89.45	89.26	90.11	89.46

Table 3B Representative electron microprobe analyses (EDS) of orthopyroxenes from experiments on MORB pyrolite

Run no.	C3	C4	T-2700	T-3643	T-3644	C5	C6	C7	C8	T-2738	T-2729	T-2643	T-2626	T-2663	T-2635	T-2721	T-2632	T-2708
T °C	925	925	925	925	925	925	925	925	925	975	1000	1000	1000	1000	1000	1025	1025	1050
P	5	10	15	20	25	28	30	32	32	5	4	10	25	27	28	7	27	7
SiO_2	55.07	54.79	54.24	54.40	54.46	55.95	56.73	57.20	56.61	54.38	53.95	54.33	55.17	55.08	54.60	54.65	55.01	53.72
TiO_2	0.09	0.10	0.00	0.17	0.09	0.10	0.09	0.09	0.08	0.00	0.00	0.00	0.00	0.00	0.00	0.00	0.00	0.00
Al_2O_3	2.64	4.11	5.12	4.40	4.56	2.56	1.59	1.16	1.69	6.00	5.83	4.91	4.28	4.72	5.36	5.18	4.32	6.07
Cr_2O_3	0.58	0.15	0.46	0.26	0.25	0.31	0.49	0.21	0.37	0.38	0.63	0.46	0.41	0.48	0.36	0.41	0.53	0.79
FeO	8.07	8.27	7.00	7.50	7.60	7.08	6.71	6.41	6.84	6.71	6.99	7.06	6.82	6.48	6.95	6.90	6.46	6.80
NiO	0.14	0.14	0.00	0.00	0.15	0.18	0.14	0.21	0.09	0.00	0.00	0.00	0.00	0.00	0.00	0.00	0.00	0.00
MgO	32.19	31.69	31.70	32.57	32.59	33.36	33.73	34.21	34.14	31.71	31.74	32.57	32.56	32.37	32.14	32.15	32.84	31.68
CaO	1.21	0.76	1.48	0.70	0.31	0.47	0.52	0.50	0.18	0.82	0.86	0.67	0.76	0.87	0.59	0.71	0.84	0.94
Total	100.00	100.00	100.00	100.00	100.00	100.00	100.00	100.00	100.00	100.00	100.00	100.00	100.00	100.00	100.00	100.00	100.00	100.00
(O = 6)																		
Si	1.924	1.908	1.883	1.890	1.891	1.938	1.961	1.973	1.956	1.880	1.871	1.884	1.908	1.903	1.888	1.891	1.902	1.863
Ti	0.002	0.003	0.000	0.004	0.002	0.003	0.002	0.002	0.002	0.000	0.000	0.000	0.000	0.000	0.000	0.000	0.000	0.000
Al	0.109	0.169	0.210	0.181	0.187	0.105	0.065	0.047	0.069	0.245	0.239	0.201	0.175	0.193	0.219	0.212	0.177	0.249
Cr	0.016	0.004	0.013	0.007	0.007	0.008	0.013	0.006	0.010	0.010	0.017	0.013	0.011	0.013	0.010	0.011	0.014	0.022
Fe	0.236	0.241	0.203	0.218	0.221	0.205	0.194	0.185	0.198	0.194	0.203	0.205	0.197	0.187	0.201	0.200	0.187	0.197
Ni	0.004	0.004	0.000	0.000	0.004	0.005	0.004	0.006	0.002	0.000	0.000	0.000	0.000	0.000	0.000	0.000	0.000	0.000
Mg	1.676	1.645	1.641	1.686	1.686	1.722	1.738	1.759	1.758	1.633	1.640	1.683	1.679	1.666	1.657	1.658	1.692	1.637
Ca	0.045	0.028	0.055	0.026	0.012	0.017	0.019	0.019	0.007	0.030	0.032	0.025	0.028	0.032	0.022	0.026	0.031	0.035
Total	4.012	4.002	4.005	4.012	4.010	4.003	3.997	3.998	4.002	3.993	4.001	4.010	3.999	3.994	3.997	3.998	4.003	4.002
Mg#	87.66	87.23	88.97	88.55	88.43	89.36	89.96	90.49	89.89	89.39	89.00	89.16	89.48	89.90	89.18	89.25	90.06	89.25

Run no.	T-2649	T-2712	T-2818	T-2817	T-2677	T-2646	T-2709	T-2813	T-2717	T-2624	T-2693	T-2672	T-2703	T-2665	T-2814	T-2616	T-2705	T-2621
T °C	1050	1050	1050	1050	1050	1075	1075	1075	1075	1075	1075	1075	1075	1100	1100	1100	1100	1100
P	10	15	18	20	26	10	15	18	20	23	24	25	26	10	18	20	24	27
SiO_2	54.81	54.80	54.49	54.68	55.05	54.48	54.61	54.47	54.50	55.11	55.03	54.59	55.21	54.19	54.25	54.65	54.13	54.78
TiO_2	0.00	0.00	0.00	0.00	0.00	0.00	0.00	0.00	0.00	0.00	0.00	0.00	0.00	0.00	0.00	0.00	0.00	0.00
Al_2O_3	5.00	5.06	5.50	5.19	4.99	5.28	5.16	5.86	5.43	5.18	4.79	5.49	4.69	5.94	5.85	5.67	5.97	5.30
Cr_2O_3	0.44	0.50	0.45	0.43	0.37	0.43	0.52	0.40	0.43	0.41	0.50	0.53	0.62	0.64	0.42	0.45	0.92	0.41
FeO	6.88	6.86	6.80	6.55	6.89	6.71	6.54	6.44	6.57	6.46	6.56	6.41	6.40	6.50	6.49	6.42	6.35	6.51
NiO	0.00	0.00	0.00	0.00	0.00	0.00	0.00	0.00	0.00	0.00	0.00	0.00	0.00	0.00	0.00	0.00	0.00	0.00
MgO	32.10	31.85	31.87	32.37	32.10	32.24	32.15	31.88	32.06	31.83	32.18	32.14	32.32	31.57	32.09	31.90	31.63	32.22
CaO	0.77	0.93	0.89	0.78	0.60	0.86	1.02	0.95	1.01	1.01	0.94	0.84	0.76	1.16	0.90	0.91	1.00	0.78
Total	100.00	100.00	100.00	100.00	100.00	100.00	100.00	100.00	100.00	100.00	100.00	100.00	100.00	100.00	100.00	100.00	100.00	100.00
(O = 6)																		
Si	1.896	1.897	1.885	1.890	1.902	1.885	1.889	1.881	1.885	1.902	1.902	1.886	1.906	1.875	1.875	1.887	1.872	1.892
Ti	0.000	0.000	0.000	0.000	0.000	0.000	0.000	0.000	0.000	0.000	0.000	0.000	0.000	0.000	0.000	0.000	0.000	0.000
Al	0.204	0.207	0.225	0.212	0.204	0.216	0.211	0.239	0.222	0.211	0.196	0.224	0.191	0.243	0.239	0.231	0.244	0.216
Cr	0.012	0.014	0.012	0.012	0.010	0.012	0.014	0.011	0.012	0.011	0.014	0.014	0.017	0.018	0.011	0.012	0.025	0.011
Fe	0.199	0.199	0.197	0.189	0.199	0.194	0.189	0.186	0.190	0.187	0.190	0.185	0.185	0.188	0.188	0.185	0.184	0.188
Ni	0.000	0.000	0.000	0.000	0.000	0.000	0.000	0.000	0.000	0.000	0.000	0.000	0.000	0.000	0.000	0.000	0.000	0.000
Mg	1.655	1.643	1.643	1.667	1.653	1.662	1.657	1.641	1.652	1.638	1.657	1.654	1.663	1.628	1.653	1.641	1.631	1.658
Ca	0.029	0.034	0.033	0.029	0.022	0.032	0.038	0.035	0.037	0.037	0.035	0.031	0.028	0.043	0.033	0.034	0.037	0.029
Total	3.995	3.993	3.996	3.999	3.991	4.001	3.998	3.994	3.998	3.986	3.993	3.995	3.990	3.995	4.000	3.991	3.993	3.994
Mg#	89.26	89.22	89.31	89.80	89.25	89.54	89.75	89.82	89.69	89.78	89.73	89.93	90.00	89.64	89.81	89.85	89.87	89.82

Table 3C Representative electron microprobe analyses (EDS) of clinopyroxenes from experiments on MORB pyrolite

Run no.	C3	C4	T-2700	T-3643	T-3644	C5	C6	C7	C8	T-2738	T-2729	T-2643	T-2626	T-2663	T-2635	T-2721	T-2632	T-2708
T °C	925	925	925	925	925	925	925	925	925	975	1000	1000	1000	1000	1000	1025	1025	1050
P	5	10	15	20	25	28	30	32	32	5	4	10	25	27	28	7	27	7
SiO_2	53.06	52.10	52.78	51.65	52.17	54.11	54.32	54.93	54.10	51.70	51.00	51.53	52.89	53.54	53.52	51.25	53.27	51.36
TiO_2	0.19	0.32	0.26	0.43	0.36	0.34	0.21	0.14	0.11	0.32	0.40	0.32	0.33	0.36	0.37	0.36	0.30	0.42
Al_2O_3	3.16	4.18	3.19	4.43	4.37	2.72	2.26	2.69	2.51	4.80	5.29	5.54	4.97	4.27	3.82	5.40	4.25	6.07
Cr_2O_3	0.63	0.51	0.36	0.42	0.58	0.66	1.11	0.69	1.00	0.52	1.19	0.59	0.65	1.06	0.93	0.69	1.03	0.62
FeO	3.94	3.42	3.29	3.88	3.48	2.83	2.68	2.72	2.53	3.89	4.01	3.68	3.28	2.97	3.00	3.53	3.15	3.61
NiO	0.12	0.19	0.00	0.23	0.19	0.16	0.15	0.25	0.00	0.00	0.00	0.00	0.00	0.00	0.00	0.00	0.00	0.00
MgO	18.27	17.39	16.87	16.59	16.95	17.35	16.89	17.32	18.20	16.41	16.75	17.35	17.00	17.14	16.81	16.66	17.27	17.67
CaO	20.50	21.75	23.00	22.24	21.18	20.90	21.30	19.77	20.02	22.09	21.11	20.65	20.04	19.45	20.49	21.78	19.53	19.96
Na_2O	0.13	0.14	0.26	0.13	0.71	0.93	1.08	1.49	1.54	0.27	0.25	0.34	0.83	1.21	1.06	0.33	1.20	0.29
Total	100.00	100.00	100.00	100.00	100.00	100.00	100.00	100.00	100.00	100.00	100.00	100.00	100.00	100.00	100.00	100.00	100.00	100.00
(O = 6)																		
Si	1.924	1.894	1.921	1.885	1.897	1.956	1.967	1.979	1.953	1.884	1.859	1.869	1.909	1.929	1.934	1.865	1.923	1.858
Ti	0.005	0.009	0.007	0.012	0.010	0.009	0.006	0.004	0.003	0.009	0.011	0.009	0.009	0.010	0.010	0.010	0.008	0.011
Al	0.135	0.179	0.137	0.191	0.188	0.116	0.097	0.115	0.107	0.207	0.228	0.237	0.212	0.182	0.163	0.232	0.181	0.259
Cr	0.018	0.015	0.010	0.012	0.017	0.019	0.032	0.020	0.028	0.015	0.034	0.017	0.019	0.030	0.027	0.020	0.029	0.018
Fe	0.119	0.104	0.100	0.119	0.106	0.085	0.081	0.082	0.076	0.119	0.122	0.112	0.099	0.090	0.091	0.107	0.095	0.109
Ni	0.004	0.006	0.000	0.007	0.006	0.005	0.004	0.007	0.000	0.000	0.000	0.000	0.000	0.000	0.000	0.000	0.000	0.000
Mg	0.987	0.942	0.915	0.903	0.918	0.935	0.912	0.930	0.979	0.891	0.910	0.938	0.915	0.921	0.905	0.904	0.929	0.952
Ca	0.797	0.847	0.897	0.870	0.825	0.810	0.827	0.763	0.775	0.863	0.825	0.802	0.775	0.751	0.793	0.849	0.756	0.774
Na	0.009	0.010	0.018	0.009	0.050	0.065	0.076	0.104	0.108	0.019	0.018	0.024	0.058	0.085	0.074	0.023	0.084	0.020
Total	3.999	4.005	4.007	4.006	4.016	4.000	4.001	4.002	4.030	4.006	4.007	4.007	3.996	3.997	3.998	4.011	4.006	4.002
Mg#	89.21	90.06	90.14	88.39	89.66	91.63	91.83	91.89	92.77	88.26	88.16	89.36	90.23	91.14	90.90	89.37	90.71	89.71

Run no.	T-2649	T-2712	T-2818	T-2817	T-2677	T-2646	T-2665	T-2709	T-2813	T-2717	T-2624	T-2693	T-2672	T-2703	T-2814	T-2616	T-2705	T-2621
T °C	1050	1050	1050	1050	1050	1075	1100	1075	1075	1075	1075	1075	1075	1075	1100	1100	1100	1100
P	10	15	18	20	26	10	10	15	18	20	23	24	25	26	18	20	24	27
SiO_2	51.35	51.72	51.91	51.16	53.31	51.31	51.32	51.21	51.71	51.90	51.67	52.26	51.85	52.50	51.25	51.73	52.19	53.17
TiO_2	0.39	0.28	0.45	0.45	0.39	0.48	0.42	0.42	0.34	0.29	0.35	0.41	0.36	0.39	0.41	0.36	0.38	0.31
Al_2O_3	6.16	5.69	5.76	6.27	4.72	6.02	6.40	5.72	6.05	6.36	6.54	5.72	5.92	5.65	6.58	6.54	6.35	5.05
Cr_2O_3	0.65	0.78	0.76	0.68	1.15	1.07	0.75	0.81	0.71	0.85	0.66	1.40	0.98	0.67	0.71	0.78	0.91	1.00
FeO	3.53	3.33	3.50	3.92	3.01	3.11	3.99	3.48	3.61	3.21	3.75	3.15	3.27	3.15	3.81	3.59	3.50	3.17
NiO	0.00	0.00	0.00	0.00	0.00	0.00	0.00	0.00	0.00	0.00	0.00	0.00	0.00	0.00	0.00	0.00	0.00	0.00
MgO	16.92	17.05	16.64	16.62	16.65	16.69	16.58	17.06	16.63	16.72	16.27	16.53	16.97	16.78	16.32	16.40	16.05	16.67
CaO	20.71	20.80	20.43	20.33	19.38	20.88	20.18	20.88	20.35	19.89	19.96	19.45	19.76	19.57	20.29	19.80	19.27	19.31
Na_2O	0.29	0.35	0.55	0.57	1.39	0.44	0.36	0.42	0.59	0.78	0.80	1.08	0.89	1.29	0.63	0.80	1.35	1.32
Total	100.00	100.00	100.00	100.00	100.00	100.00	100.00	100.00	100.00	100.00	100.00	100.00	100.00	100.00	100.00	100.00	100.00	100.00
(O = 6)																		
Si	1.860	1.873	1.879	1.857	1.922	1.860	1.860	1.859	1.873	1.874	1.870	1.888	1.875	1.895	1.858	1.870	1.885	1.917
Ti	0.011	0.008	0.012	0.012	0.011	0.013	0.011	0.011	0.009	0.008	0.010	0.011	0.010	0.011	0.011	0.010	0.010	0.008
Al	0.264	0.244	0.246	0.269	0.201	0.258	0.274	0.245	0.259	0.271	0.280	0.244	0.253	0.241	0.282	0.279	0.271	0.215
Cr	0.019	0.022	0.022	0.020	0.033	0.031	0.021	0.023	0.020	0.024	0.019	0.040	0.028	0.019	0.020	0.022	0.026	0.029
Fe	0.107	0.101	0.106	0.119	0.091	0.094	0.121	0.106	0.109	0.097	0.114	0.095	0.099	0.095	0.116	0.109	0.106	0.096
Ni	0.000	0.000	0.000	0.000	0.000	0.000	0.000	0.000	0.000	0.000	0.000	0.000	0.000	0.000	0.000	0.000	0.000	0.000
Mg	0.914	0.920	0.898	0.899	0.895	0.901	0.896	0.923	0.898	0.900	0.878	0.890	0.914	0.902	0.882	0.884	0.864	0.896
Ca	0.804	0.807	0.792	0.791	0.749	0.811	0.784	0.812	0.790	0.769	0.774	0.753	0.765	0.757	0.788	0.767	0.746	0.746
Na	0.020	0.025	0.039	0.040	0.097	0.031	0.025	0.030	0.041	0.055	0.056	0.076	0.062	0.090	0.044	0.056	0.095	0.092
Total	3.998	3.999	3.994	4.006	3.999	3.998	3.993	4.010	3.999	3.998	3.999	3.997	4.006	4.010	4.002	3.997	4.003	3.999
Mg#	89.52	90.12	89.44	88.31	90.79	90.53	88.10	89.73	89.14	90.27	88.55	90.34	90.24	90.47	88.42	89.06	89.10	90.36

Table 3D Representative electron microprobe analyses (EDS) of pargasitic amphiboles from subsolidus experiments on MORB pyrolite

Run no.	C3	C4	T-2700	T-3643	T-3644	C5	C6	T-2738	T-2643	T-2626	T-2663	T-2721	T-2632	T-2649	T-2712	T-2818	T-2817	T-2624
T °C	925	925	925	925	925	925	925	975	1000	1000	1000	1025	1025	1050	1050	1050	1050	1075
P	5	10	15	20	25	28	30	5	10	25	27	7	27	10	15	18	20	23
SiO_2	47.18	47.72	44.63	43.05	44.10	46.43	46.17	45.47	44.88	45.04	45.36	43.55	45.29	43.16	44.25	43.16	43.86	44.20
TiO_2	1.23	0.48	0.53	0.78	0.76	0.83	0.82	0.89	0.79	0.70	0.66	0.88	0.74	1.03	0.84	0.93	0.87	0.91
Al_2O_3	11.20	12.52	13.80	15.22	14.18	12.57	12.20	13.85	14.11	13.65	12.60	15.94	13.07	16.60	15.39	15.39	15.07	14.74
Cr_2O_3	1.11	0.90	1.10	0.75	0.97	0.99	1.13	1.06	0.97	1.47	1.05	0.89	1.06	1.30	1.07	1.08	0.89	0.89
FeO	4.66	3.91	4.85	5.62	4.83	3.76	4.04	4.41	4.45	3.74	4.04	4.86	3.97	3.90	3.97	4.48	4.01	4.16
NiO	0.18	0.16	0.00	0.24	0.35	0.33	0.27	0.00	0.00	0.00	0.00	0.00	0.00	0.00	0.00	0.00	0.00	0.00
MgO	20.00	19.62	20.51	19.80	18.72	19.31	19.66	19.15	19.47	19.72	20.94	20.30	19.47	18.71	18.88	19.40	19.30	18.98
CaO	10.75	11.11	10.46	10.16	11.04	10.40	10.27	11.23	10.99	10.16	9.71	9.32	10.44	10.70	10.73	10.43	10.59	10.47
Na_2O	1.70	1.59	2.12	2.39	3.05	3.38	3.44	1.94	2.34	3.52	3.64	2.26	3.95	2.60	2.86	3.13	3.41	3.65
Total	98.00	98.00	98.00	98.00	98.00	98.00	98.00	98.00	98.00	98.00	98.00	98.00	98.00	98.00	98.00	98.00	98.00	98.00
(O = 23)																		
Si	6.601	6.632	6.270	6.084	6.237	6.505	6.484	6.368	6.298	6.321	6.369	6.099	6.372	6.054	6.204	6.084	6.167	6.219
Ti	0.129	0.050	0.056	0.083	0.081	0.087	0.086	0.094	0.083	0.074	0.070	0.093	0.078	0.109	0.089	0.099	0.092	0.096
Al(IV)	1.399	1.368	1.730	1.916	1.763	1.495	1.516	1.632	1.702	1.679	1.631	1.901	1.628	1.946	1.796	1.916	1.833	1.781
Al(VI)	0.454	0.687	0.561	0.626	0.606	0.586	0.509	0.660	0.638	0.585	0.459	0.737	0.545	0.806	0.754	0.648	0.672	0.669
Cr	0.122	0.098	0.122	0.084	0.108	0.110	0.126	0.117	0.108	0.163	0.117	0.099	0.118	0.144	0.119	0.120	0.099	0.099
Fe	0.545	0.454	0.570	0.664	0.571	0.440	0.474	0.517	0.522	0.439	0.474	0.569	0.467	0.458	0.466	0.528	0.472	0.489
Ni	0.020	0.018	0.000	0.027	0.040	0.038	0.031	0.000	0.000	0.000	0.000	0.000	0.000	0.000	0.000	0.000	0.000	0.000
Mg	4.170	4.064	4.294	4.170	3.946	4.031	4.114	3.997	4.072	4.124	4.382	4.237	4.083	3.911	3.945	4.076	4.044	3.980
Ca	1.611	1.655	1.575	1.538	1.673	1.561	1.545	1.685	1.653	1.528	1.461	1.399	1.574	1.608	1.612	1.575	1.596	1.578
Na(M4)	0.000	0.000	0.000	0.000	0.000	0.147	0.115	0.000	0.000	0.087	0.038	0.000	0.135	0.000	0.016	0.000	0.026	0.088
Na(A)	0.460	0.429	0.578	0.655	0.836	0.772	0.823	0.527	0.637	0.871	0.953	0.614	0.943	0.707	0.762	0.856	0.904	0.908
Total	15.512	15.456	15.756	15.848	15.861	15.772	15.823	15.597	15.713	15.871	15.953	15.747	15.943	15.743	15.762	15.903	15.904	15.908
Mg#	88.43	89.94	88.28	86.26	87.36	90.15	89.66	88.56	88.63	90.38	90.23	88.16	89.73	89.53	89.45	88.53	89.56	89.05

Table 3E Representative electron microprobe analyses (EDS) of garnets from experiments on MORB pyrolite

Run no.	T-3644	C5	C6	C7	C8	T-2626	T-2635	T-2632	T-2817	T-2677	T-2717	T-2624	T-2693	T-2672	T-2703	T-2705	T-2621
T °C	925	925	925	925	925	1000	1000	1025	1050	1050	1075	1075	1075	1075	1075	1100	1100
P	25	28	30	32	32	25	28	27	20	26	20	23	24	25	26	24	27
SiO_2	41.98	41.34	41.73	40.28	41.82	42.46	42.53	42.46	42.03	42.53	42.60	41.95	42.16	42.17	42.37	42.94	42.34
TiO_2	0.26	0.39	0.58	0.42	0.35	0.23	0.32	0.35	0.25	0.32	0.28	0.35	0.18	0.31	0.47	0.28	0.39
Al_2O_3	22.61	22.11	21.71	23.67	22.01	20.89	21.75	21.88	23.25	22.18	21.49	21.85	21.81	21.93	22.03	20.50	21.05
Cr_2O_3	0.84	2.31	1.58	2.46	1.41	1.28	1.75	1.59	0.94	1.37	1.57	2.38	2.24	1.93	1.89	2.10	2.40
FeO	9.63	9.60	8.70	8.68	8.61	8.43	8.18	8.41	8.19	7.63	7.39	7.88	7.67	7.57	7.68	7.53	7.46
MgO	18.65	17.32	18.01	17.48	18.77	20.38	19.57	19.44	18.86	19.71	19.84	18.68	20.09	19.71	19.21	20.09	20.11
CaO	6.03	6.93	7.69	7.01	7.03	6.33	5.90	5.87	6.47	6.25	6.83	6.92	5.84	6.39	6.34	6.56	6.24
Total	100.00	100.00	100.00	100.00	100.00	100.00	100.00	100.00	100.00	100.00	100.00	100.00	100.00	100.00	100.00	100.00	100.00
(O = 12)																	
Si	3.003	2.980	2.998	2.896	2.995	3.032	3.029	3.025	2.990	3.021	3.031	2.999	3.002	3.003	3.016	3.060	3.018
Ti	0.014	0.021	0.032	0.023	0.019	0.012	0.017	0.019	0.013	0.017	0.015	0.019	0.010	0.017	0.025	0.015	0.021
Al	1.912	1.884	1.843	2.012	1.863	1.763	1.831	1.842	1.955	1.862	1.807	1.846	1.835	1.845	1.853	1.726	1.774
Cr	0.047	0.131	0.090	0.140	0.080	0.072	0.099	0.090	0.053	0.077	0.088	0.135	0.126	0.109	0.106	0.118	0.135
Fe	0.576	0.579	0.523	0.522	0.516	0.504	0.487	0.501	0.487	0.453	0.440	0.471	0.457	0.451	0.457	0.449	0.445
Mg	1.989	1.861	1.928	1.873	2.003	2.169	2.077	2.064	2.000	2.087	2.104	1.991	2.132	2.092	2.038	2.134	2.137
Ca	0.462	0.535	0.592	0.540	0.540	0.484	0.450	0.448	0.493	0.476	0.521	0.530	0.446	0.488	0.484	0.501	0.477
Total	8.003	7.991	8.004	8.005	8.015	8.037	7.990	7.990	7.992	7.992	8.006	7.991	8.008	8.004	7.979	8.003	8.006
Ca	15.26	17.99	19.45	18.41	17.64	15.34	14.94	14.87	16.55	15.78	16.99	17.72	14.68	16.09	16.23	16.25	15.59
Mg	65.71	62.56	63.37	63.82	65.49	68.71	68.90	68.50	67.10	69.19	68.66	66.53	70.26	69.03	68.42	69.20	69.87
Fe	19.03	19.45	17.18	17.77	16.87	15.95	16.16	16.63	16.35	15.03	14.35	15.75	15.05	14.88	15.35	14.55	14.54
Mg#	77.54	76.28	78.67	78.21	79.52	81.16	81.00	80.47	80.41	82.15	82.71	80.86	82.36	82.27	81.68	82.62	82.77

Table 3F Representative electron microprobe analyses (EDS) of spinels and plagioclase from experiments on MORB pyrolite

Run no.	C4	T-2700	T-3643	T-2712	Run no.	C3
T °C	925	925	925	1050	T °C	925
P	10	15	20	15	P	5
TiO_2	0.12	0.29	0.48	0.27	SiO_2	43.47
Al_2O_3	50.94	40.81	47.10	53.70	Al_2O_3	36.98
Cr_2O_3	17.04	26.00	10.75	13.09	Fe_2O_3	0.62
FeO	13.39	15.34	17.28	10.63	MgO	0.52
MnO	0.16	0.00	0.00	0.00	CaO	17.62
NiO	0.49	0.41	0.83	0.35	Na_2O	0.79
MgO	17.30	17.15	18.30	21.96	K_2O	0.00
Total	100.00	100.00	100.00	100.00	Total	100.00
(O = 4)					(O = 8)	
Ti	0.002	0.006	0.010	0.005	Si	2.003
Al	1.623	1.343	1.562	1.643	Al	2.014
Cr	0.363	0.573	0.239	0.268	Fe + 3	0.021
Fe + 3	0.009	0.072	0.179	0.079	Mg	0.036
Fe + 2	0.293	0.285	0.226	0.151	Ca	0.870
Mn	0.004	0.000	0.000	0.000	Na	0.071
Ni	0.011	0.009	0.019	0.007	K	0.000
Mg	0.695	0.712	0.765	0.847	Total	5.015
Total	3.000	3.000	3.000	3.000		
					An	92.49
Mg#	70.32	71.40	77.18	84.86		
Cr#	18.29	29.89	13.25	14.02		

3. Modal variation in pargasite-bearing MORB pyrolite

Modal proportions of phases in pargasitic amphibole-bearing MORB pyrolite (MPY-40%OL) were calculated for subsolidus run products, in which pargasitic amphiboles were well analysed by electron microprobe, using the generalized mixing model proposed by Le Maitre (1979). In the mixing model, total iron was assumed to be FeO and all analysed components were fitted. The calculated modal proportions, in weight per cent, are presented in Table 4. Phases with very small grain size such as spinel, plagioclase, could not always be analysed. The best available compositions from other runs at the closest pressure and temperature were selected: the spinel composition from the run T-2712 for calculations of T-2812 and T-2818, the spinel from T-2700 for T-2643, the spinel from C4 and the plagioclase from C3 for T-2738, and the garnet from T-2635 for T-2663.

The experimental charge at $P = 15$ kbar, $T = 925$ °C (T-2700), which was used as starting material, initially contained 35% pargasitic amphibole, 6% clinopyroxene, 34% orthopyroxene, 24% olivine, and 1% spinel. In the higher temperature runs at $P = 15$ kbar, the modal amount of pargasitic amphibole diminishes while the modal amount of clinopyroxene and olivine clearly increases, for example T-2712 at $T = 1050$ °C, $P = 15$ kbar, compared with the $T = 925$ °C run T-2700 at $P = 15$ kbar. The higher pressure runs in the garnet stability field are characterized by marked decreases in amphibole, orthopyroxene and spinel, and by a large increase in the modal amounts of clinopyroxene and olivine as well as crystallization of garnet, compared with the lower pressure runs.

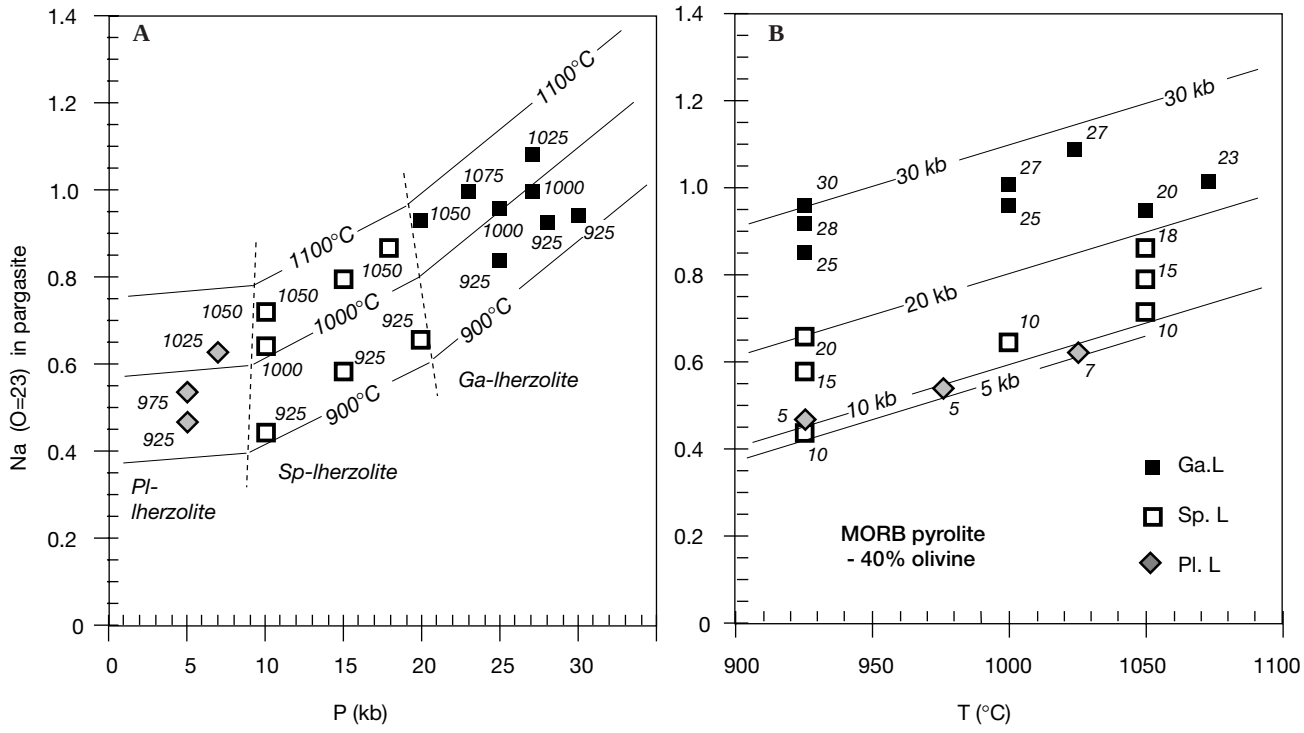

Fig. 4A, B Compositional variation of Na(A + M4) for pargasitic amphiboles from amphibole-bearing MORB pyrolite experiments as a function of pressure (kbar) (**A**) and temperature (°C) (**B**). Isotherms ($T = 900$, 1000, 1100 °C) and isobars ($P = 10$, 20, 30 kbar) are shown as *solid lines*. *Dotted lines* in **A** show boundaries among the plagioclase, spinel, and garnet lherzolite fields. Symbols of *solid diamonds* are pargasitic amphiboles from the plagioclase lherzolite field (*Pl.L*), *open squares* from the spinel lherzolite field (*Sp.L*), and *solid squares* from the garnet lherzolite field (*Ga.L*)

Figure 6A and B shows the modal variation of pargasitic amphibole from the MORB pyrolite experiments. A decrease in the modal proportions with temperature is immediately apparent from Fig. 6A. In the spinel and garnet lherzolite fields the modal proportion of amphibole below the solidus suggests that the amphibole breakdown reactions occur gradually and continuously throughout the subsolidus field, involving the production of clinopyroxene and olivine (plus garnet in the garnet lherzolite field). The breakdown reaction of amphibole becomes more active at the solidus, producing a melt phase, and then the amphibole is eliminated at the amphibole stability limit, approximately 15 °C higher than the solidus. The decline in modal pargasitic amphibole with pressure is clearly defined from the series of runs at constant temperature at $T = 925$ °C, 1000 °C and 1050 °C within the spinel and garnet stability fields (Fig. 6B).

In the plagioclase lherzolite field, the composition of pargasite shows decreasing tremolite and increasing pargasite solid solution with increase in temperature (Figs. 4 and 5). Our data are insufficient to determine details of compositional changes with pressure within the plagioclase lherzolite field and the calculated modal abundances give good mass balance for the 975 °C, 5 kbar run but not for the 925 °C, 5 kbar run. We infer that modal pargasite increases rapidly with increasing pressure at constant temperature within the plagioclase lherzolite (Figs. 6B and 8A). We also infer that modal pargasite decreases with increasing temperature at $T > 900$ °C at 5 kbar (Figs. 6A and 8B). A more detailed study of the plagioclase lherzolite field and transition to the spinel lherzolite field, in the 2 to 15 kbar pressure range, is required to document changes in pargasite, plagioclase and spinel compositions. However our data, illustrated in Figs. 6 and 8, suggest that maximum modal pargasite is attainable near $P = 10$ kbar at the plagioclase to spinel lherzolite transition.

Discussion

1. Effect of bulk rock alkali content on pargasitic amphibole stability

The stability field of pargasitic amphibole is bounded by very low pressure dehydration reactions, by melting reactions at low and intermediate pressure, and by high pressure dehydration reactions to olivine, garnet, pyroxenes, ilmenite and phlogopite assemblages. The solidus, and thus the high temperature limit of amphibole stability in the peridotite-H_2O system, occurs at higher temperature with $a_{H_2O} < 1$. Holloway (1973) demonstrated that the maximum temperature stability for pargasitic amphiboles at $P = 8$ kbar was at $X_{H_2O} = 0.4$.

Figure 7 compares the stability field of pargasitic amphibole for MORB pyrolite with those determined for three different lherzolitic compositions, using the

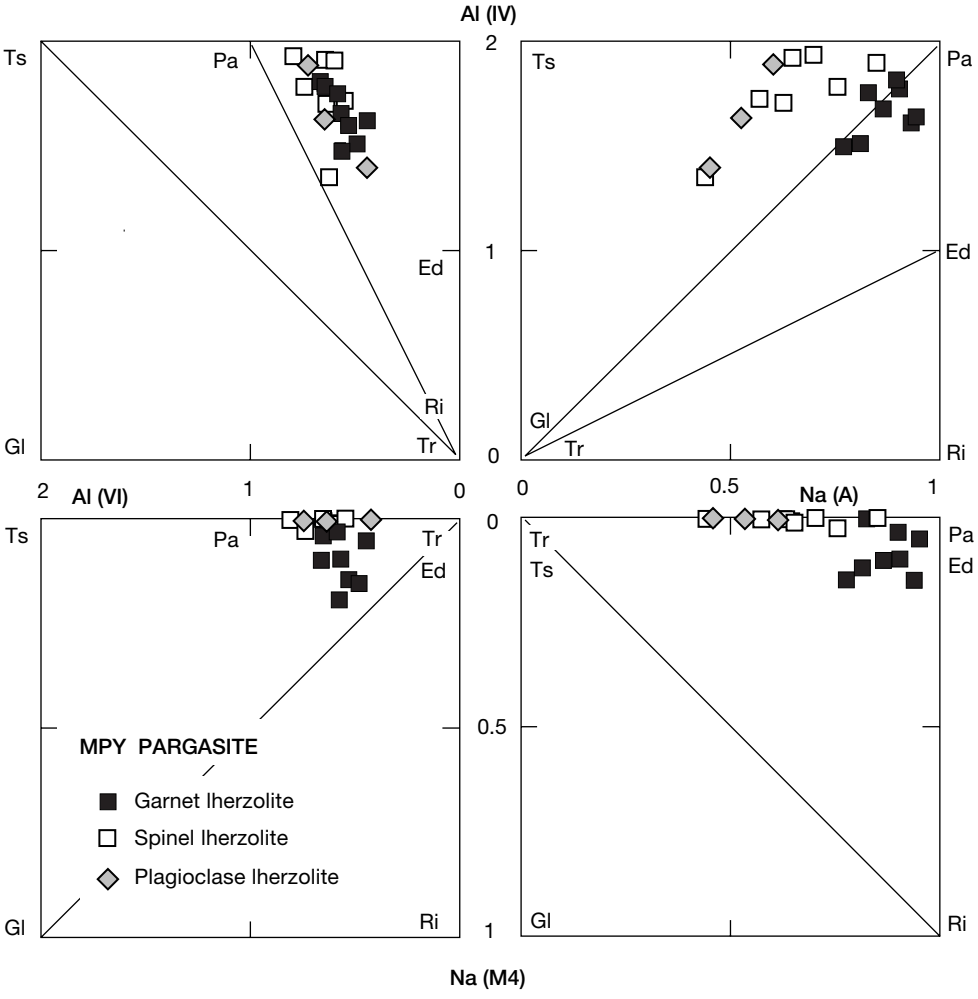

Fig. 5 Plots of Al(IV) versus Na(A) (*upper right*), Al(IV) versus Al(VI) (*upper left*), Na(M4) versus Na(A) (*right bottom*), and Na(M4) versus Al(VI) (*left bottom*) for pargasitic amphiboles experimentally produced from peridotite with MORB pyrolite-40% olivine composition in equilibrium with plagioclase lherzolite (*grey diamonds*), spinel lherzolite (*open squares*) and garnet lherzolite (*solid squares*). Note the compositional change from tremolitic pargasite in plagioclase lherzolite to pargasitic in spinel lherzolite, and that the richterite substitution becomes more active in the garnet lherzolite facies

Table 4 Modal % of phases in subsolidus runs of MORB pyrolite −40% olivine, calculated by mass balance (see text). Note that modal abundances in MORB pyrolite may be calculated by adding 40% olivine and recalculating to 100% (see Fig. 8A). (*Ol* olivine, *Opx* orthopyroxene, *Cpx* clinopyroxene, *Pa* pargasite, *Sp* spinel, *Ga* garnet, *Pl* Plagioclase)

Run no.	*T* °C	*P* kbar	Ol	Opx	Cpx	Pa	Ga	Sp	Pl
C3	925	5	32.1	29.0	3.5	26.5	–	0.0	8.9
C4	925	10	28.1	24.9	1.0	45.4	–	0.6	–
T-2700	925	15	24.2	33.6	6.0	35.2	–	1.0	–
T-3643	925	20	21.2	38.5	10.8	28.0	–	1.5	–
T-3644	925	25	25.9	31.2	10.9	23.8	8.2	–	–
C5	925	28	28.3	27.6	9.8	22.0	12.2	–	–
C6	925	30	27.9	24.8	9.5	17.7	20.0	–	–
C7	925	32	29.0	24.8	18.5	–	27.7	–	–
C8	925	32	27.3	24.5	18.3	–	29.9	–	–
T-2738	975	5	28.1	32.2	7.9	28.9	–	0.8	2.1
T-2643	1000	10	24.6	33.4	8.8	32.0	–	1.3	–
T-2626	1000	25	28.4	25.1	14.3	15.7	16.5	–	–
T-2663	1000	27	29.8	22.8	17.3	10.2	19.9	–	–
T-2712	1050	15	25.3	36.2	14.6	21.3	–	2.6	–
T-2818	1050	18	24.5	37.6	16.4	18.9	–	2.6	–
T-2817	1050	20	26.3	33.1	17.1	13.9	8.6	1.1	–
T-2624	1075	23	29.2	28.5	15.4	13.7	13.3	–	–

same experimental techniques. All starting materials contained 0.6% H_2O, held in pargasitic amphibole (+ phlogopite in a K-enriched composition). The differences in shapes and the positions of amphibole breakdown curve can be attributed to differences in bulk compositions and thus in pargasitic amphibole compositions.

The pargasitic amphibole stability for Hawaiian pyrolite composition has been determined to lie at a pressure between 29 and 30 kbar at 1000 °C, and at a temperature between 1150 °C and 1170 °C at 25 kbar (Green 1973). The amphibole stability in Northern Hessian Depression peridotite composition (Mengel and Green 1989) lies at $P = 28$ kbar, $T = 1050$ °C, and shows a similar temperature limit to that of Hawaiian pyrolite. Wallace and Green (1991) reported that pargasitic amphibole stability in the Tinaquillo lherzolite composition lies at a temperature of 1025 °C at pressures between 20 and 25 kbar, and up to 1000 °C at 15 kbar. The reduction in the maximum temperature stability of pargasitic amphibole in the Tinaquillo lherzolite composition relative to the Hawaiian pyrolite was attributed to bulk rock alkali and titanium contents (Wallace and Green 1991). The pargasitic amphibole stability in the MORB pyrolite composition lies at

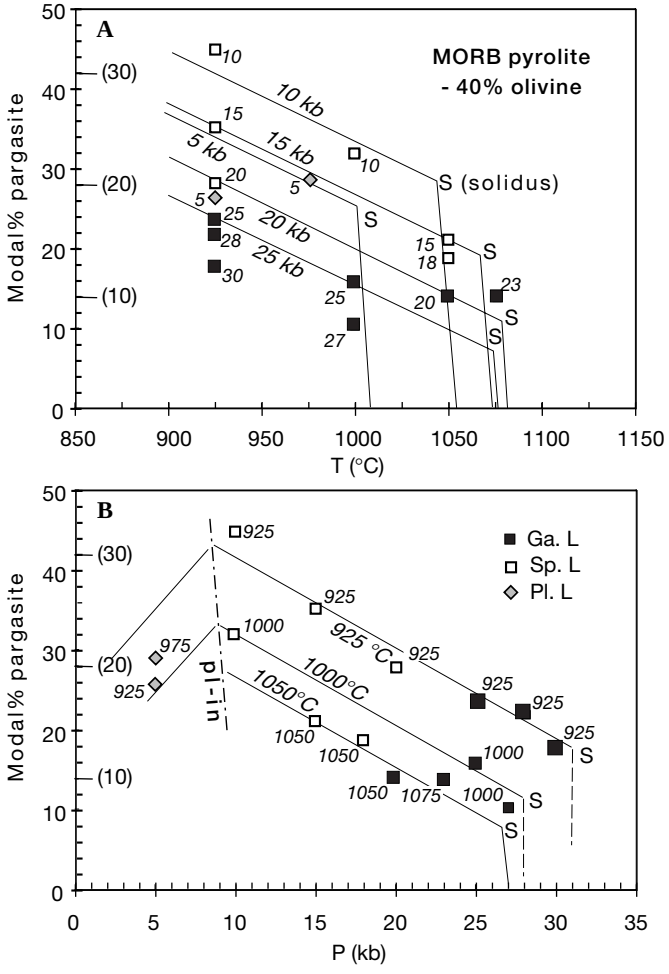

Fig. 6A, B Calculated modal proportions of pargasitic amphiboles (wt%) experimentally produced in the subsolidus runs, plotted against temperature (T °C) (**A**) and pressure (*P* kbar) (**B**). The proportions decrease with increasing temperature in the spinel and garnet lherzolite fields. Isobars (10, 15, 20, and 25 kbar) and isotherms ($T = 925$, 1000, 1050 °C) lined-up by the isobaric and isothermal runs, respectively, showing smooth, parallel lines decreasing toward the solidus (*s*). The pargasitic amphibole disappears at the stability limit within 15 °C above the solidus. The figures in brackets on the "Y" axis refer to modal composition in "MORB-pyrolite", rather than the "MORB pyrolite-40% olivine" composition

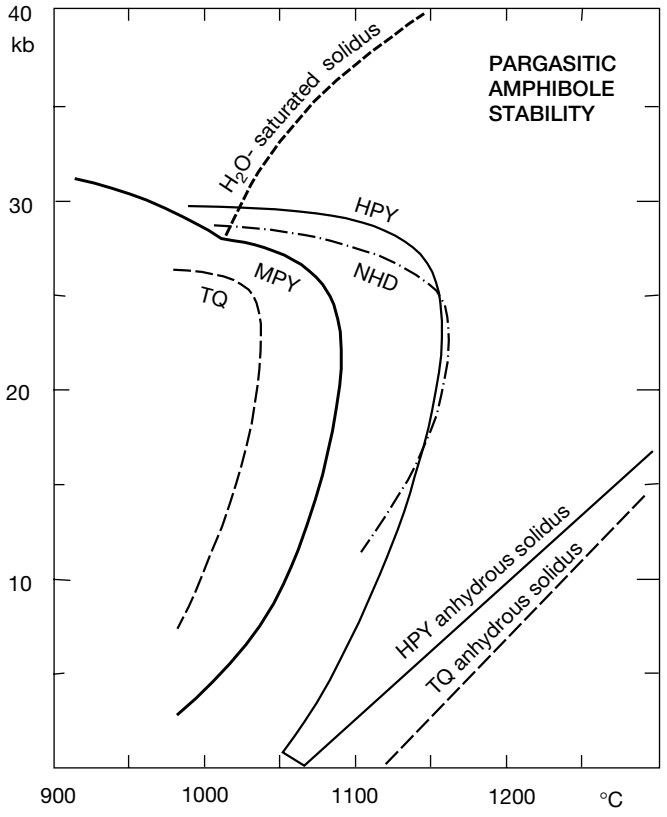

Fig. 7 Comparison of pargasitic amphibole stability for MORB pyrolite (*heavy solid line*, *MPY*; this work) with that of Hawaiian pyrolite (*light solid line*, *HPY*; Green 1973), Northern Hessian Depression peridotite (*dashed line with dot*, *NHD*; Mengel and Green 1989), and Tinaquillo lherzolite (*dashed line*, *TQ*; Wallace and Green 1991), experimentally produced under water-undersaturated conditions using the same method. Data for anhydrous solidi after Green (1973) and Jaques and Green (1980)

$P = 30$ kbar, $T = 925$ °C; at $P = 28$ kbar, $T = 1000$ °C; and at $T = 1075$ °C at pressures of 18 to 25 kbar (Fig. 1). The upper pressure and temperature stability limit of amphibole in the MORB pyrolite composition lies between that of the Tinaquillo lherzolite composition and those of the Hawaiian pyrolite and NHD peridotite compositions (Fig. 7).

The maximum pressure stability of pargasitic amphibole around $T = 1000$ °C shifts with increasing total alkali contents of the bulk rock composition, e.g. from 26 kbar (TQ-40%OL, 0.33 wt% $Na_2O + K_2O$), 28 kbar (MPY-40%OL, 0.66 wt% $Na_2O + K_2O$), 28–29 kbar (NHD + 1.5%PHL-60%OL, 0.78 wt% $Na_2O + K_2O$), and up to 29–30 kbar (HPY-40%OL, 1.17 wt% $Na_2O + K_2O$). The maximum temperature stability of pargasitic amphibole also expands from 1025 °C to 1150 °C with increasing alkali contents of the bulk rock composition. The stability of amphibole in NHD peridotite shows a higher temperature limit than those in the other peridotitic compositions. It is possible that the relatively higher K_2O content of the NHD peridotite (0.43 wt%) stabilizes amphibole to higher temperatures than that which would be expected from the total alkali contents.

The results of this experimental study are in good agreement with the explanation of bulk rock composition control on amphibole stability by Wallace and Green (1991) and with the experimental results in the system CaO-MgO-Al_2O_3-SiO_2-Na_2O-H_2O (Cawthorn 1976). We also confirm the conclusion of Wallace and Green (1991) that the temperatures of the dehydration solidi of pargasitic lherzolites are directly rather than inversely proportional to their "fertility" as measured by Na + K content – this intuitively surprising result will facilitate mass transfer by melting and melt migration in inhomogeneous lherzolite at $T = 950$–1150 °C. In high temperature lherzolites at low water activities, a melt fraction occurring in a refractory composition may mi-

grate and become fixed in pargasite-rich "fertile" lenses or bands because of the higher solidus temperature of (Na + K)-enriched pargasite lherzolites.

2. Na and Al contents in pargasitic amphibole

Examination of previous experimental work on pargasitic amphiboles demonstrates an increase in Na in A-site occupancy with increasing temperature (Holloway and Burnham 1972; Helz 1973, 1976, 1979; Green 1973, 1976; Spear 1981; Gilbert et al. 1982). Helz (1973) noted a tight linear correlation between the A-site occupancy by Na and the Al^{IV} content. However there has not been any opportunity for a systematic survey of amphibole composition in a constant bulk composition over a range of pressure and temperature. The data obtained for MORB pyrolite composition and illustrated in Fig. 4A and B can be used to deduce a pattern of Na content of pargasitic amphibole as a function of pressure and temperature (Fig. 8B). The contours of Fig. 8B are derived from the linear interpolations in Fig. 4 and imply that the Na content is positively correlated with both pressure and temperature and in the presence of garnet the sensitivity to pressure is enhanced.

In a similar way, the positive correlation between Al content and temperature has been established in earlier studies (Helz 1973; Mysen and Boettcher 1975b; Spear 1981; Gilbert et al. 1982) and has been attributed to increasing tschermakite solid solution. The effects of pressure on total Al and Al^{VI} substitution are not well established although the analyses of both Spear (1981) and Gilbert et al. (1982) show increase in Al^{VI} as pressure increases. Figure 5 shows that Al^{IV} and Al^{VI} increase with increasing pressure from the plagioclase to spinel lherzolite fields and decrease with increasing pressure from the spinel to garnet lherzolite fields. The data indicate a maximum content of Al close to the dehydration solidus in the spinel stability field. These changes are attributed to increasing tschermakite content with increasing pressure from the plagioclase to spinel lherzolite fields (i.e. increase in Al^{IV} and Al^{VI}) and to increasing richterite content with increasing pressure [i.e. decrease in Al^{IV} and Al^{VI} with increase in Na(A) and Na(M4)].

3. Pargasite breakdown reactions

Analyses of phases in the $P = 15$ kbar, $T = 925$ °C experiment (starting materials) allow us to calculate the modal composition at this pressure and temperature, establishing that 35% of pargasite is present in the MORB pyrolite-40% olivine composition. Higher pressure and temperature experiments show decreasing modal amphibole (Table 4, Figs. 6 and 8) accompanied by the changes in amphibole composition noted previously. Pargasitic amphibole and clinopyroxene are the only Na-bearing phases in the spinel or garnet lherzolite assemblages at subsolidus conditions. The data demon-

Fig. 8A, B Pressure (kbar) and temperature (°C) relationship of the modal proportion in wt% (**A**) and the Na (O = 23) content (**B**) of pargasitic amphiboles from MORB pyrolite-40% olivine experiments. Isopleths and modal abundance contours were fitted from the compositional variation trends in Figs. 3 and 4. In **A**, the *bracketed figure on the contour* is the modal abundance in MORB pyrolite (i.e. with 40% olivine restored)

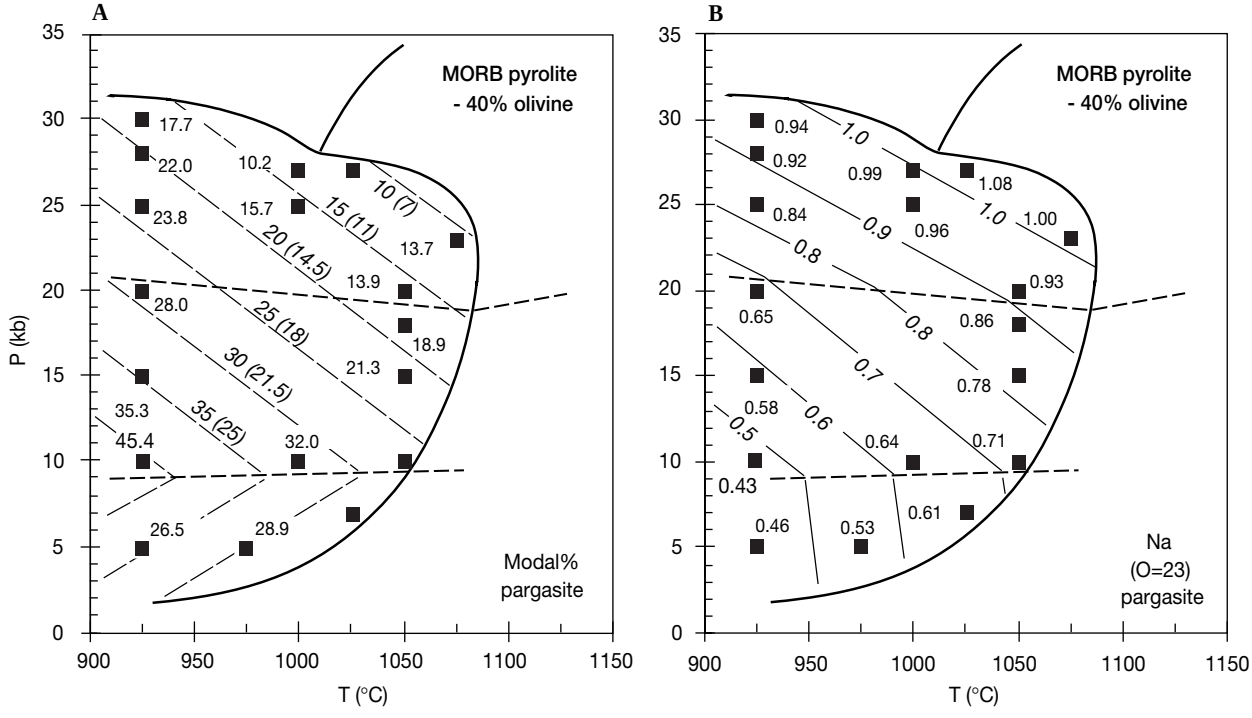

strate that the amphibole breakdown reactions are continuous reactions and occur over a P, T range, quantified in Figs. 4, 5, 6 and 8. Recognizing the complex nature of the pargasite solid solution, we may use the modal and compositional changes in mineral compositions to infer the component reactions.

In the plagioclase lherzolite field, the tremolite component decreases with increasing temperature and the pargasite component increases with increase in both temperature and pressure. In the spinel lherzolite field the pargasite component is replaced by richterite towards higher pressure. The effect is more evident in the garnet lherzolite field, where there is a decrease in Tschermak's component and a further increase in richterite. The modal and mineral compositional data show that enstatite is decreasing, garnet is increasing, and jadeite solid solution in clinopyroxene is increasing over the same pressure interval, suggesting the reaction;

$$3\text{pa} + (\text{CaAl}_2\text{SiO}_6)_{\text{cpx}} + 10\text{en} \rightarrow \text{ri} + \text{jd} + (2\text{gr} + 3\text{py}) + 4\text{fo} + 2\text{H}_2\text{O} \ .$$

The pargasite breakdown also occurs as part of the spinel lherzolite to garnet lherzolite transition as:

$$3\text{pa} + \text{sp} + \text{di} + \text{en} \rightarrow \text{ri} + \text{jd} + (2\text{gr} + 3\text{py}) + 5\text{fo} + 2\text{H}_2\text{O} \ .$$

The high pressure limit of the pargasitic amphibole is expressed as a richterite breakdown reaction, e.g. ri + $2(\text{CaAl}_2\text{SiO}_6)_{\text{cpx}} \rightarrow$ 2jd + gr + en + 2fo + H_2O, or more plausibly to include a pargasitic amphibole breakdown reaction, i.e. (3pa + ri) + ($5\text{MgAl}_2\text{SiO}_6$ + 8en) $\rightarrow$ 5jd + $7(\text{gr}_{0.33}\text{py}_{0.67})$ + 8fo + $4\text{H}_2\text{O}$.

The melting reactions involve the disappearance of 10–30% pargasitic amphibole over a temperature interval as small as 15 °C (Fig. 6). At lower pressure, Boyd (1959), Holloway (1973) and others (Holloway and Burnham 1972; Helz 1973, 1976; Francis 1976) have established that pargasite melts incongruently to Di + Fo + Sp + liquid. The present study shows that the solidus of the amphibole-bearing lherzolite used in this study is not a simple dehydration solidus in which a fluid-absent, pargasite-bearing lherzolite melts to spinel or garnet lherzolite mineralogy and water-rich melt. The data obtained show that pargasite-bearing lherzolite undergoes continuous reactions under sub-solidus conditions such that the composition of amphibole at the solidus varies with pressure as well as temperature.

The data of Tables 3 and 4 and the plots of amphibole compositions in Figs. 4 and 5 and modal abundances of Figs. 6 and 8A, may be combined to deduce the reactions between the components of pargasite solid solution and other phases which occur as functions of pressure and temperature along the constant modal pargasite contours of Fig. 8A. These reactions must conserve H_2O if we assume, to a first approximation, that pargasitic amphibole does not change water content over the P, T field examined. The reaction from low to high pressure along the modal pargasite contour is:

$$2\text{pa} + \text{ts} + 4\text{di} + 16\text{en} \rightarrow \text{ri} + 2\text{tr} + 5(\text{gr}_{0.33}\text{py}_{0.67}) + 3\text{fo} \ .$$

This reaction is deduced from compositions along the 20% and 15% pargasite contours, i. e. compositional and modal abundance data for experiments at $P = 28$ kbar and 30 kbar, $T = 925$ °C (with 22% and 18% pargasite respectively) compared with those at $P = 15$ kbar and 18 kbar, $T = 1050$ °C (with 21% and 14% pargasite respectively) supports this reaction as the principal pressure effect on amphibole composition in a closed system in the garnet lherzolite field.

4. H_2O released by pargasite breakdown

The observations on mineral compositions and modal abundances, and the continuous reactions inferred in the preceding section, require the release of water from the 15 kbar, 925 °C starting material in both higher temperature and pressure experiments. In addition, the patterns of modal variation and phase compositions at $P > 15$ kbar are consistent among the 925 °C runs, irrespective of whether the charges contained 2.0 wt% H_2O or the 15 kbar, 925 °C starting mix (0.6 wt% H_2O). It therefore becomes necessary for us critically to examine our charges to ascertain whether the solidus possibly coincided with the water-saturated solidus at $P > 15$ kbar or whether our optical and electron microprobe evidence for a "dehydration-solidus" ($a_{\text{H}_2\text{O}} < 1$) at $T_{\max} = 1075$ °C can be confirmed. Previous work on the Hawaiian pyrolite, NHD and Tinaquillo lherzolite compositions under water-saturated conditions ($a_{\text{H}_2\text{O}} \sim 1$) had defined solidi at $T = 970$–1000 °C over the pressure range of 5–25 kbar.

We used scanning electron microscopy (SEM) to examine the freshly broken surface of the experiments (Fig. 2). They were clearly porous with excellent euhedral crystal faces against voids (i.e. vapour filled cavities). Similarly, experiments at $T = 1000$ °C ($P = 25$–30 kbar), $T = 1050$ °C ($P = 15$–20 kbar) and $T = 1075$ °C ($P = 23$ kbar) were also porous with euhedral crystal faces against cavities. By contrast, experiments at $T = 1075$ °C ($P = 10$–20 kbar, 24–26 kbar) and at $T > 1075$ °C were non-porous and showed fractured crystal faces and minor conchoidal quenched glass, interstitially. The scanning electron microscopy images thus confirmed the location of the solidus in Fig. 1, and established the presence of a vapour phase at $T = 925$ °C and throughout the pargasite lherzolite P, T field for which modal pargasite was <35 wt% approximately.

As an additional technique, we used ion-beam thinning on experiments at $T = 1000$ °C and 1050 °C ($P = 10$ kbar) and at $T = 1000$ °C ($P = 27$ kbar) and then examined the products by transmission electron microscopy (TEM) (Fig. 3). The TEM technique also enabled semi-quantitative energy dispersive X-ray fluorescence analyses of the ion-beam thinned charge. By this technique we identified quench amphibole, "mica"

(phyllo-silicate) and siliceous, alkaline and Fe rich glass as outgrowths and intercrystalline pools in the above-solidus run at $T = 1050$ °C, $P = 10$ kbar. By contrast, in the subsolidus runs at $T = 1000$ °C ($P = 10$ kbar, 27 kbar), we found no quench crystal outgrowths or phases and observed only extremely delicate thin-film deposits and "spheres" along some grain boundaries (Fig. 3A). Energy dispersive analyses showed high silica, alkalis, and sulphur in these glass films and we interpret this material as vapour-phase quench.

One further observation is relevant to the interpretation of subsolidus runs. In run C7 ($P = 32$ kbar), pargasite is absent and the clinopyroxene contains 1.49 wt% Na_2O, the highest observed in any assemblages. However, the modal abundance of clinopyroxene (18.5%) gives an Na_2O content for the bulk composition of 0.39 wt% Na_2O, much less than the actual composition (0.66%). By contrast pargasite and clinopyroxene in runs C5 ($P = 28$ kbar) and C6 ($P = 30$ kbar) account for ~0.7 to 0.8% Na_2O and there is no mass balance problem for Na_2O. A repeat run (Run No. C8) at $P = 32$ kbar, $T = 925$ °C with lower water content (i.e. all water originally contained in pargasite, approximately 0.6 wt% H_2O in bulk composition) also produced clinopyroxene with 1.54 wt% Na_2O and mass balance requires the presence of an additional Na-rich phase. The SEM observations of freshly broken surfaces revealed extremely fine needles and surface depositions on crystals. Energy dispersive analysis indicated high Na, Si and S and the possibility of Na_2SiO_3-rich quench crystals can not be excluded. We infer that a fluid phase, rich in Na_2O and possibly a brine or "carbonatite" was present in the 32 kbar, 925 °C experiments. The modal analyses and mass balance results for the lower pressure experiments suggest much lower Na_2O content in the fluid phase.

To summarize, our detailed examination of charges by SEM and TEM techniques confirms the location of the solidus as in Fig. 1 and that the melting reactions include the disappearance of pargasite over a temperature interval <15 °C. It should be noted that at $P = 25$ kbar, $T = 1075$ °C an olivine-rich basanite magma contains approximately 10–12 wt% H_2O (figure derived from liquidus depression experiments summarized in Green (1973)). Thus an estimate of degree of melting immediately above the amphibole-out boundary is roughly 5% (0.6% H_2O in bulk composition) and the melt increases from 0 to 5% over <15 °C in our experiments. Our experimental techniques are such that a vapour phase is present below the "dehydration solidus" but the activity of water in this vapour phase is <1. This occurs because initial loading of capsules traps 30–50% by volume of air and traces of sulphur, carbon and halogens may result from our sample preparation process. The TEM images also confirm that the vapour phase contains dissolved components which precipitate as thin glass films or as vapour quench, alkali-rich needles (from the run C8 in particular). With $a_{H_2O} < 1$, the solidus is defined by the (pargasite + vapour = hydrous melt + lherzolite) reactions. Taylor and Green (1988) used $CH_4 + H_2O$ fluid in buffered capsules to demonstrate that pargasitic amphibole could exist to $T = 1190$ °C at $P = 25$ kbar (at lower f_{O_2} than the present experiments) and its upper thermal stability in Hawaiian pyrolite composition included breakdown to a phlogopite-bearing but melt-absent garnet lherzolite assemblage. The experiments conducted here simulate conditions under which natural amphibole-bearing lherzolites may begin melting upon temperature increase or pressure decrease. The activity of water along the solidus is clearly <1 at pressures less than 28 kbar and we have shown that this dehydration solidus is dependent on bulk peridotite composition and the amphibole composition.

5. Porosity and connectivity of subsolidus fluid phase

The SEM image of Fig. 2A and particularly the TEM images of Fig. 3A and B are relevant to discussions of porosity and permeability of mantle lherzolite in the presence of an aqueous fluid. Recent studies (Watson and Brenan 1987; Watson et al. 1991; Mibe et al. 1998) interpret fluid distribution and connectivity in olivine-rich materials in terms of dihedral angle (the angle formed by two intersecting walls of a pore or tubule formed by three or more juxtaposed crystals). Mibe et al. (1998) obtained dihedral angles of $<60°$ at 30 and 50 kbar which they contrast with values of $>65°$ obtained by Watson et al. (1991) at 10 kbar. Mibe et al. 1998 infer high connectivity and permeability for aqueous fluid at 30 and 50 kbar and attribute the change from low to high pressure to the increased solubility of silicate components in fluid at high pressure.

In our experiments we have evidence for significant silicate solubility in aqueous fluid at 10 kbar, 1000 °C (Fig. 3A) and have provided evidence for Na-, Si- and S-rich precipitates from fluid at 32 kbar, 925 °C. However, at both 10 kbar and 27 kbar (Fig. 3A and B), pore geometry is dominated by crystal faces and there is no suggestion of significant difference in pore characteristics. In both cases, the insight from TEM on pore morphology suggests that the use of polished surfaces with the resolution of SEM will not adequately measure dihedral angles and furthermore that fluid exists in discrete pores bounded in large part by crystal faces. The dihedral angle intersection between crystal phases is determined by relative crystal orientation and cannot be interpreted as a simple property of an olivine/aqueous fluid pair, for example. We believe that it is premature to infer high permeability of aqueous fluids in the upper mantle at $T > 900$ °C on the basis of interpretation of dihedral angles measured on polished surfaces. We note that fluid contents in our samples are $<0.5\%$ (maximum water content in charges is 0.6–0.7%) and that at 10 kbar there is significant silicate solubility in the fluid.

Applications to pargasite-bearing natural peridotites

1. Cooling and decompression paths and heating events observed in natural peridotites

Compositional dependence of amphibole on T, P and bulk rock composition has been discussed in some literature on basaltic magmas (e.g. Helz 1973, 1976; Cawthorn 1976; Spear 1981). Stephenson (1977) showed a different range of Ti and Al^{VI} contents of hornblendes between amphibolite and granulite facies gneisses from the south coast of Western Australia. Hammarstrom and Zen (1986) collated data on calcic amphiboles from some calc-alkalic plutonic complexes showing a similar total Al–Al^{IV} trend with systematic pressure effect and mentioned that total Al content of hornblende is useful as an empirical igneous geobarometer. In examples of amphibole-bearing peridotites, however, the amphibole itself has not been a sensitive indicator for estimation of equilibration pressure and temperature. In most cases, P-T history of alpine-type peridotites emplaced within crustal terrains and of upper mantle-derived xenoliths have been estimated from their aluminous phase paragenesis or by pressure and temperature calculations using the coexisting phases other than amphiboles. New data on pargasitic amphiboles presented in Figs. 4, 5, and 8 show compositional dependence on P and T and therefore provide constraints on cooling and decompression paths and "heating" events for natural peridotites.

Some orogenic lherzolites carry pargasitic amphiboles recrystallized at lower pressure and temperature than the primary conditions. Secondary pargasites in the Lizard lherzolite have a low Na_2O content (1.87–2.45 wt%; Green 1964). Pargasitic amphiboles (1.87–3.01 wt% Na_2O), which are considered to be equilibrated at a relatively low P-T condition, were also reported from Finero (Cawthorn 1975) and Alpe Arami (Ernst 1978) in northern Italy. The Na_2O-rich pargasitic amphiboles (3.25–4.06 wt% Na_2O) coexisting with garnet in the Ronda peridotite (Obata 1980) suggest a high pressure and temperature equilibration. Compositional zoning of pargasitic amphiboles has been reported from garnet peridotite in Norway (Medaris 1984) and from garnet-spinel lherzolite in northern Italy (Obata and Morten 1987). The zoned amphiboles have an Na_2O-rich pargasitic core rimmed by Na_2O-poor tremolite or hornblende, suggesting a decompressional cooling history.

It is also possible from the compositional dependence of pargasitic amphibole to recognize "heating" events of peridotite xenoliths which have been heated in the upper mantle prior to capture by the ascending host magmas. Takahashi (1980) described a "preheated" xenolith from Ichinomegata in northern Japan. Pargasitic amphiboles in the preheated spinel lherzolite are more sodic (2.96 wt% Na_2O) and more aluminous (14.92 wt% Al_2O_3) than the other types of amphiboles (2.01–2.34 wt% Na_2O, 12.26–12.98 wt% Al_2O_3) in equilibration with lower temperature olivine and pyroxenes. Such a heating event in mantle-derived xenoliths has also been reported as a "reheating event" from the Malaita alnoites in Solomon Islands (Neal and Nixon 1985). The reheating was linked to a garnet breakdown reaction resulting in a secondary assemblage of clinopyroxene, amphibole and spinel. The amphibole has an extremely sodic (4.72 wt% Na_2O) and aluminous (15.26 wt% Al_2O_3) pargasite composition, which indicates both higher temperature and higher pressure equilibration.

From this brief literature survey, there appears to be potential for direct application of the experimental data presented herein to aid in interpretation of P, T history of natural lherzolites.

2. Model for pargasite peridotite wall limiting mantle upwelling to define the volcanic front of subduction zones

It has become widely accepted that generation of arc magma at convergent plate boundaries is intimately associated with subduction of oceanic lithosphere and that dehydration of the subducted slab and hydration of the mantle peridotite wedge are important processes in magma genesis (e.g. Nicholls and Ringwood 1973; Wyllie and Sekine 1982; Green et al. 1987; Kushiro 1987). Tatsumi (1986, 1989) proposed a specific model for location of the volcanic front of subduction zones. In this model, partial melting of the mantle peridotite wedge is caused by H_2O released from hydrated peridotite dragged along the downgoing slab. The position of the volcanic front is attributed to the pargasite dehydration reaction within this peridotite at 30 kbar (100 km), producing H_2O-rich melting in the overlying mantle wedge.

Based on the stability of pargasitic amphibole in MORB pyrolite composition (Fig. 1), a plausible model of pargasite distribution in the upper mantle beneath an island arc is shown in Fig. 9. The maximum depth of pargasite distribution lies around 90 km ($P = 28$–30 kbar) in the mantle peridotite. As the upper layer of the subducting slab itself has a basaltic composition, and would contain modal quartz in garnet amphibolite or eclogite assemblages, the amphiboles in the slab become unstable at shallower level, approximately 70 km (Gilbert et al. 1982; Poli 1993; Poli and Schmidt 1995). However, pargasitic amphibole may remain as a stable phase in the lithospheric peridotites beneath the crust of frontal arc and fore-arc regions and in the uppermost mantle peridotites of back-arc regions. Highly sodic pargasites containing 3–4 wt% Na_2O are restricted to high temperature, approaching the silicate solidus and the maximum pressure for amphibole stability.

As shown in Fig. 9, migration of H_2O from the slab into the overlying wedge produces effects which are strongly dependent on the local temperature. In cool regions close to the trench, stability of serpentine,

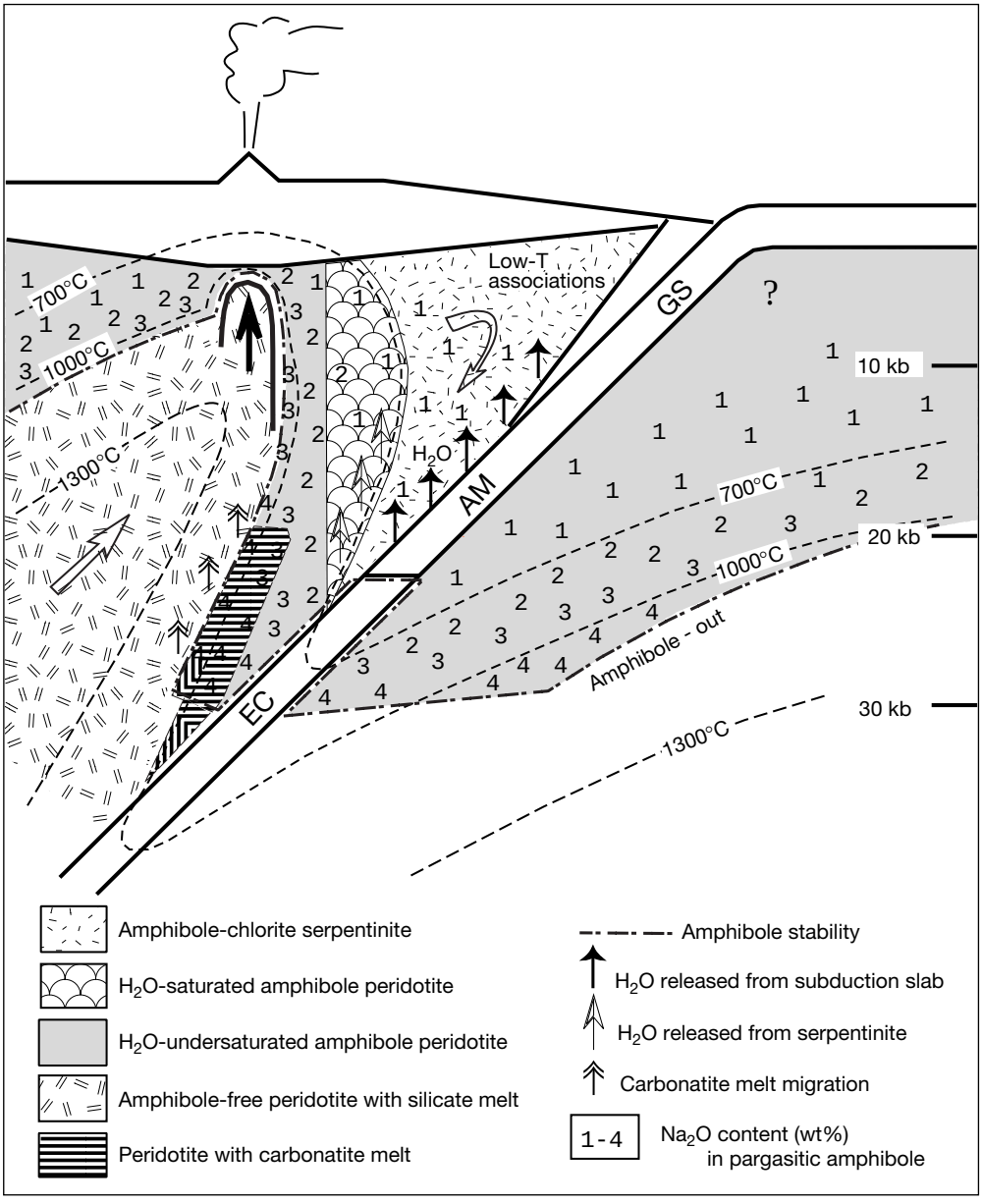

Fig. 9 Schematic model of subduction zone, showing pargasitic amphibole distribution in the upper mantle peridotite (*shaded area*), deduced from the experimental results for MORB pyrolite. *Numbers* indicate the plausible contents of Na_2O (wt%) in pargasitic amphiboles, illustrating distribution of high Na_2O pargasite in the peridotite wall facing mantle diapiric upwelling and the region of silicate melting limited by the pargasite amphibole-bearing lherzolite solidus, thus defining the volcanic front

chlorite, talc, diopside and tremolite enables extensive hydration (>10% contained H_2O in former lherzolite), which, if pervasive, will lead to low density and tectonic extrusion rather than subduction of serpentinized lithosphere. Pargasite lherzolite with ~25–30% pargasite (containing ~1% Na_2O in the pargasite) may form in the region, particularly in higher temperatures of the wedge or with low a_{H_2O} in the penetrative fluids. In the schematic model of Fig. 9, H_2O-rich fluids released by dehydration reaction are presented as rising vertically in the deforming lherzolite of the mantle wedge. A temperature of 650–700 °C is assumed somewhat arbitrarily for the dehydration of serpentine/chlorite assemblages in lherzolite leading to an overlying region of water-saturated pargasite lherzolite in which 20–30% pargasite (1–2% Na_2O) is present.

If the subduction process drags pargasite lherzolite to deeper levels, there is partial dehydration leading to decreasing pargasite abundance and increasingly sodic pargasite. The *P*, *T* field of the subduction wedge may be contoured for the sodium content of pargasite. Pargasite is not stable beyond 30 kbar. However, the detailed study does not support the simple expression of Tatsumi's model (1986, 1989) in which the volcanic front (~100 km above the subduction zone) is attributed to pargasite breakdown at 30 kbar pressure. The continu-

ous nature of the pargasitic breakdown reactions implies release of H_2O at depths < 100 km in the wedge counterflow or drag model.

The silicate solidus in Fig. 9 is drawn at 1050–1075 °C and represents the dehydration solidus of MORB pyrolite. The position of the silicate solidus in the mantle wedge is primarily determined by the temperature distribution and secondarily by the sensitive control of the peridotite solidus by a_{H_2O}, pargasite stability and bulk composition. An additional complexity is the high probability that the fluid released from slab reactions and from peridotite devolatilization reactions is a C—H—O fluid, dominated under the oxidized conditions of the subducted slab environment, by $CO_2 + H_2O$. The study of carbonate stability in lherzolite and of the P, T field for primary carbonatite melts (Wyllie et al. 1983; Wallace and Green 1988; Green and Wallace 1988; Falloon and Green 1990) shows that there is a P, T field for carbonatite melt in equilibrium with pargasite lherzolite from $P = 22$–30 kbar, $T = 935$–1075 °C approximately and with pargasite-free lherzolite from $P > 30$ kbar, $T = 935$–1025 °C. Because of the temperature inversion within the mantle wedge, the region of carbonatite melt lies spatially below the region of silicate melting. In Fig. 9 carbonatite melts are depicted as migrating into the silicate melting region where they dissolve in the more voluminous silicate melt with moderate to high carbonate solubility at 20–30 kbar, providing one of the potential geochemical components postulated for the source characteristics of island arc magmas (i.e. one of the "slab" metasomatic agents as discussed by Sweeney et al., 1992).

The roles of pargasite stability, carbonatitic and silicate melt regions, illustrated in Fig. 9, are general features of any model but their specific application is sensitively controlled by the P, T distribution modelled for the subduction and mantle wedge environments. Figure 9 is schematic, noting alternative temperature distributions of geophysical models (Toksöz et al. 1971; Peacock 1990; Davies and Stevenson 1992; Furukawa 1993; Davies 1994). The dip of the subduction slab, rate of subduction, presence of segmentation and rifting perpendicular to the trench, or transform faults terminating arc-trench systems, perturb the P, T distributions, and thus the spatial characteristics of regions of partial melting. It is argued that the source of primitive magmas in island arc settings lies within the envelope of silicate melting schematically depicted in Fig. 9. Volcanism is envisaged as a consequence of upwelling of mantle from within this region (see schematic "diapir" of Fig. 9). The limit to partial melting, and thus to magma genesis either by melt segregation within a diapiric upwelling, or via porous flow and melt pooling in an upwelling region, is defined by the solidus reaction (hydrous melt + lherzolite → pargasite lherzolite). We infer that the volcanic front of island arcs is defined by the position of this solidus in the temperature inversion of the wedge above the subduction zone, producing a depth/temperature envelope which is the source region for island arc magmatism. Within this envelope, heterogeneity of source composition reflects recycling of old lithosphere and injection of back-arc asthenosphere, and is further complicated by wedge metasomatism to introduce pargasite and the potential for carbonatite melt migration.

Acknowledgements This work was carried out mostly at the University of Tasmania during the tenure of a post-doctoral exchange programme between the Japan Society for the Promotion of Science and the Australian Academy of Science to K. Niida. Financial support was also provided by Australian Research Grant Scheme funds to D. H. Green. This experimental work has benefited greatly from the technical assistance of K. L. Harris and W. Jablonski, the constructive comments of T. J. Falloon, Ai Yang, A. J. Crawford, and S. M. Eggins, and discussion on chemistry of experimentally produced amphiboles with W. R. Taylor, M. E. Wallace and N. Odling. Additional series of experiments at $T = 925$ °C have been done at the Research School of Earth Science of the Australian National University and have benefited from the technical assistance of Nick Ware, Bill Hibberson, Mike Shelley, and Paul Willis. Nick Ware and John Fitzgerald obtained the SEM and TEM images respectively. The paper benefited greatly from constructive reviews by Bernard Evans and Max Schmidt. These contributions are warmly acknowledged.

References

Ballhaus C, Berry RF, Green DH (1990) Oxygen fugacity controls in the Earth's upper mantle. Nature 348: 437–440

Boyd FR (1959) Hydrothermal investigations of the amphiboles. In: Abelson PH (ed) Researches in geochemistry. John Wiley and Sons, New York, pp 377–396

Cawthorn RG (1975) The amphibole peridotite–metagabbro complex, Finero, northern Italy. J Geol 83: 437–454

Cawthorn RG (1976) Melting relations in part of the system CaO-MgO-Al_2O_3-SiO_2-Na_2O-H_2O under 5 kbar pressure. J Petrol 17: 44–72

Dautria JM, Liotard JM, Cabanes N, Girod M, Briqueu L (1987) Amphibole-rich xenoliths and host alkali basalts: petrogenetic constraints and implications on the recent evolution of the upper mantle beneath Ahaggar (Central Sahara, Southern Algeria). Contrib Mineral Petrol 95: 133–144

Davies JH (1994) Lateral water transport across a dynamic mantle wedge: a model for subduction zone magmatism. In: Ryan MP (ed) Magmatic systems. Academic Press Inc, London, pp 197–221

Davies JH, Stevenson DJ (1992) Physical model of source region of subduction zone volcanics. J Geophys Res 97: 2037–2070

Dawson JB, Smith JV (1982) Upper-mantle amphiboles: a review. Mineral Mag 45: 35–46

Ernst WG (1978) Petrochemical study of lherzolitic rocks from the Western Alps. J Petrol 19: 341–392

Fabriès J, Figueroa O, Lorand J-P (1987) Petrology and thermal history of highly deformed mantle xenoliths from the Montferrier basanites, Languedoc, Southern France. A. Comparison with ultramafic complexes from the North Pyrenean Zone. J Petrol 28: 887–919

Falloon TJ, Green DH (1987) Anhydrous partial melting of MORB pyrolite and other peridotite compositions at 10 kbar: implications for the origin of primitive MORB glasses. Mineral Petrol 37: 181–219

Falloon TJ, Green DH (1988) Anhydrous partial melting of peridotite from 8 to 35 kbar and the petrogenesis of MORB. J Petrol Spec Lithosphere Issue: 379–414

Falloon TJ, Green DH (1990) Solidus of carbonated fertile peridotite under fluid-saturated conditions. Geology 18: 195–199

Falloon TJ, Green DH, Hatton CJ, Harris KL (1988) Anhydrous partial melting of a fertile and depleted peridotite from 2 to 30 kbar and application to basalt petrogenesis. J Petrol 29: 1257–1282

Field SW, Haggerty SE, Erlank AJ (1989) Subcontinental metasomatism in the region of Jagersfontein, South Africa. In: Kimberlites and related rocks. Geol Soc Aust Spec Publ 14, pp 771–783

Francis DM (1976) The origin of amphibole in lherzolite xenoliths from Nunivak Island, Alaska. J Petrol 17: 357–378

Furukawa Y (1993) Magmatic processes under arcs and formation of the volcanic front. J Geophys Res 98: 8309–8319

Gilbert MC, Helz RT, Popp RK, Spear FS (1982) Experimental studies of amphibole stability. In: Veblem DR, Ribbe PH (eds), Amphiboles: petrology and experimental phase relations (Reviews in mineralogy, 9B) Mineral Soc Am, Washington, DC, pp 229–353

Green DH (1964) The petrogenesis of the high temperature peridotite intrusion in the Lizard Area, Cornwall. J Petrol 5: 134–188

Green DH (1973) Experimental studies on a model upper mantle composition at high pressure under water-undersaturated and water-saturated conditions. Earth Planet Sci Lett 19: 37–53

Green DH (1976) Experimental testing of ''equilibrium'' partial melting of peridotite under water-saturated, high pressure conditions. Can Mineral 14: 255–268

Green DH, Ringwood AE (1963) Mineral assemblages in a model mantle composition. J Geophys Res 68: 937–945

Green DH, Wallace ME (1988) Mantle metasomatism by ephemeral carbonatite melts. Nature 336: 459–462

Green DH, Hibberson WO, Jaques AL (1979) Petrogenesis of mid ocean ridge basalt. In: McElhinney MW (ed) The Earth: its origin structure and evolution. Academic Press, London, pp 265–299

Green DH, Falloon TJ, Taylor WR (1987) Mantle-derived magmas – roles of variable C—H—O fluid compositions. In: Mysen BO (ed) Magmatic processes: physicochemical principles. Geochem Soc Spec Publ 1, pp 139–154

Griffin WL, Wass SY, Hollis JD (1984) Ultramafic xenoliths from Bullenmerri and Gnotuk maars, Victoria, Australia: petrology of a subcontinental crust–mantle transition. J Petrol 25: 53–87

Hammarstrom JM, Zen E-an, (1986) Aluminium in hornblende: an empirical igneous geobarometer. Am Mineral 71: 1297–1313

Helz RT (1973) Phase relations of basalts in their melting range at $P_{H_2O} = 5$ kbar as a function of oxygen fugacity. I. Mafic phases. J Petrol 14: 249–302

Helz RT (1976) Phase relations of basalts in their melting ranges at $P_{H_2O} = 5$ kbar. II. Melt compositions. J Petrol 17: 139–193

Helz RT (1979) Alkali exchange between hornblende and melt: a temperature-sensitive reaction. Am Mineral 64: 953–965

Holloway JR (1973) The system pargasite-H_2O-CO_2: a model for melting of a hydrous mineral with a mixed-volatile fluid. 1. Experimental results to 8 kbar. Geochim Cosmochim Acta 37: 651–666

Holloway JR, Burnham CW (1972) Melting relations of basalt with equilibrium water pressure less than total pressure. J Petrol 13: 1–29

Jaques AL, Green DH (1979) Determination of liquid compositions in high-pressure melting of peridotite. Am Mineral 64: 1312–1321

Jaques AL, Green DH (1980) Anhydrous melting of peridotite at 0–15 kbar pressure and the genesis of tholeiitic basalts. Contrib Mineral Petrol 73: 287–310

Kushiro I (1970) Stability of amphibole and phlogopite in the upper mantle. Carnegie Inst Washington Yearb 68: 245–247

Kushiro I (1987) A petrological model of the mantle wedge and lower crust in the Japanese island arcs. In: Mysen BO (ed) Magmatic processes: physicochemical principles. Geochem Soc Spec Publ 1: 165–181

Kushiro I, Shimizu N, Nakamura Y, Akimoto S-I (1972) Compositions of coexisting liquid and solid phases formed upon melting of natural garnet and spinel lherzolite at high pressures: a preliminary report. Earth Planet Sci Lett 14: 19–25

Le Maitre RW (1979) A new generalized petrological mixing model. Contrib Mineral Petrol 71: 133–137

Medaris LG (1980) Petrogenesis of the Lien Peridotite and associated eclogites, Almklovdalen, Western Norway. Lithos 13: 339–153

Medaris LG (1984) A geothermobarometric investigation of garnet peridotites in the western gneiss region of Norway. Contrib Mineral Petrol 87: 72–86

Mengel K, Green DH (1989) Stability of amphibole and phlogopite in metasomatized peridotite under water-saturated and water-undersaturated conditions. In: Kimberlites and related rocks. Geol Soc Aust Spec Publ 14, pp 571–581

Mibe K, Fujii T, Yasuda A (1998) Connectivity of aqueous fluid in the Earth's upper mantle. Geophys Res Lett 25, 8: 1233–1236

Millhollen GK, Irving AJ, Wyllie PJ (1974) Melting interval of peridotite with 5.7 per cent water to 30 kbar. J Geol 82: 575–587

Mysen BO, Boettcher AL (1975a) Melting of hydrous mantle. I. Phase relations of natural peridotite at high pressure and temperature with controlled activities of water, carbon dioxide, and hydrogen. J Petrol 16: 520–548

Mysen BO, Boettcher AL (1975b) Melting of hydrous mantle. II. Geochemistry of crystals and liquids formed by anatexis of mantle peridotite at high pressures and high temperatures as a function of controlled activities of water, hydrogen, and carbon dioxides. J Petrol 16: 549–593

Neal CR, Nixon PH (1985) Spinel-garnet relationships in mantle xenoliths from the Malaita alnoites, Solomon Islands, southwestern Pacific. Trans Geol Soc S Afr 88: 347–354

Nicholls IA, Ringwood AE (1973) Effect of water on olivine stability in tholeiites and production of SiO_2-saturated magmas in the island arc environment. J Geol 81: 285–300

Nickel KG, Green DH (1984) The nature of the upper-most mantle beneath Victoria, Australia, as deduced from ultramafic xenoliths. In: Kornprobst J (ed) Kimberlites II. Elsevier, Amsterdam, pp 161–178

Obata M (1980) The Ronda peridotite: garnet-, spinel-, and plagioclase-lherzolite facies and the *P-T* trajectories of a high temperature mantle intrusion. J Petrol 21: 533–572

Obata M, Morten L (1987) Transformation of spinel lherzolite to garnet lherzolite in ultramafic lenses of the Austridic Crystalline Complex, northern Italy. J Petrol 28: 599–623

Peacock SM (1990) Fluid processes in subduction zones. Science 248: 328–337

Poli S (1993) The amphibole–eclogite transformation: an experimental study on basalt. Am J Sci 293: 1061–1107

Poli S, Schmidt MW (1995) H_2O transport and release in subduction zones: experimental constraints on basaltic and andesitic systems. J Geophys Res 100: 22299–22314

Press S, Witt G, Seck HA, Ionov D, Kovalenko VI (1986) Spinel peridotite xenoliths from the Tariat Depression, Mongolia. I. Major element chemistry and mineralogy of a primitive mantle xenolith suite. Geochim Cosmochim Acta 50: 2587–2599

Ringwood AE (1962) A model for the upper mantle, 2. J Geophys Res 67: 4473–4477

Seyler M, Mattson PH (1989) Petrology and thermal evolution of the Tinaquillo peridotite (Venezuela). J Geophys Res 94: 7629–7660

Spear FJ (1981) An experimental study of hornblende stability and compositional variability in amphibole. Am J Sci 281: 697–734

Stephenson NCN (1977) Coexisting hornblendes and biotites from Precambrian gneisses of the south coast of Western Australia. Lithos 10: 9–27

Sweeney RJ, Green DH, Sie SH (1992) Trace and minor element partitioning between garnet and amphibole and carbonatitic melt. Earth Planet Sci Lett 113: 1–14

Takahashi E (1980) Thermal history of lherzolite xenoliths. I. Petrology of lherzolite xenoliths from the Ichinomegata crater, Oga Peninsula, northeast Japan. Geochim Cosmochim Acta 44: 1643–1658

Tatsumi Y (1986) Formation of volcanic front. Geophys Res Lett 13: 717–720

Tatsumi Y (1989) Migration of fluid phases and genesis of basalt magmas in subduction zones. J Geophys Res 94: 4697–4707

Taylor WR, Green DH (1988) Measurement of reduced peridotite-C—O—H solidus and implications for redox melting of the mantle. Nature 332: 349–352

Toksöz MN, Minear JW, Julian BR (1971) Temperature field and geophysical effects of a downgoing slab. J Geophys Res 76: 1113–1138

Varne R (1970) Hornblende lherzolite and the upper mantle. Contrib Mineral Petrol 27: 45–51

Wallace ME, Green DH (1988) An experimental determination of primary carbonatite magma composition. Nature 333: 343–346

Wallace ME, Green DH (1991) The effect of bulk rock composition on the stability of amphibole in the upper mantle: implications for solidus positions and mantle metasomatism. Mineral Petrol 44: 1–19

Watson EB, Brenan JM (1987) Fluids in the lithosphere. I. Experimentally determined wetting characteristics of CO_2-H_2O fluids and their implications for fluid transport, host-rock physical properties and fluid inclusion formation. Earth Planet Sci Lett 85: 497–515

Watson EB, Brenan JM, Baker DR (1991) Distribution of fluid in the continental mantle. In: Menzies M (ed) Continental mantle. Oxford Univ Press, Oxford UK, pp 111–125

Wyllie PJ, Sekine T (1982) The formation of mantle phlogopite in subduction zone hybridization. Contrib Mineral Petrol 79: 375–380

Wyllie PJ, Huang W-L, Otto J, Byrnes AP (1983) Carbonation of peridotites and decarbonation of siliceous dolomites represented in the system CaO-MgO-SiO_2-CO_2 to 30 kbar. Tectonophysics 100: 359–388